ELSEVIER

Nuclear Physics B 611 (2001) 3–39

NUCLEAR PHYSICS B

www.elsevier.com/locate/npe

Final NOMAD results on $\nu_\mu \to \nu_\tau$ and $\nu_e \to \nu_\tau$ oscillations including a new search for ν_τ appearance using hadronic τ decays

NOMAD Collaboration

P. Astier [n], D. Autiero [h], A. Baldisseri [r], M. Baldo-Ceolin [m], M. Banner [n], G. Bassompierre [a], K. Benslama [i], N. Besson [r], I. Bird [h,i], B. Blumenfeld [b], F. Bobisut [m], J. Bouchez [r], S. Boyd [t], A. Bueno [c,x], S. Bunyatov [f], L. Camilleri [h], A. Cardini [j], P.W. Cattaneo [o], V. Cavasinni [p], A. Cervera-Villanueva [h,v], A. Chukanov [f], G. Collazuol [m], G. Conforto [h,u], C. Conta [o], M. Contalbrigo [m], R. Cousins [j], D. Daniels [c], H. Degaudenzi [i], T. Del Prete [p], A. De Santo [h,p], T. Dignan [c], L. Di Lella [h], E. do Couto e Silva [h], J. Dumarchez [n], M. Ellis [t], G.J. Feldman [c], R. Ferrari [o], D. Ferrère [h], V. Flaminio [p], M. Fraternali [o], J.-M. Gaillard [a], E. Gangler [h,n], A. Geiser [e,h], D. Geppert [e], D. Gibin [m], S. Gninenko [h,l], A. Godley [s], J.-J. Gomez-Cadenas [h,v], J. Gosset [r], C. Gößling [e], M. Gouanère [a], A. Grant [h], G. Graziani [g], A. Guglielmi [m], C. Hagner [r], J. Hernando [v], D. Hubbard [c], P. Hurst [c], N. Hyett [k], E. Iacopini [g], C. Joseph [i], F. Juget [i], M. Kirsanov [l], O. Klimov [f], J. Kokkonen [h], A. Kovzelev [l,o], A. Krasnoperov [a,f], D. Kustov [f], V.E. Kuznetsov [f,h], S. Lacaprara [m], C. Lachaud [n], B. Lakić [w], A. Lanza [o], L. La Rotonda [d], M. Laveder [m], A. Letessier-Selvon [n], J.-M. Levy [n], L. Linssen [h], A. Ljubičić [w], J. Long [b], A. Lupi [g], A. Marchionni [g], F. Martelli [u], X. Méchain [r], J.-P. Mendiburu [a], J.-P. Meyer [r], M. Mezzetto [m], S.R. Mishra [c,s], G.F. Moorhead [k], D. Naumov [f], P. Nédélec [a], Yu. Nefedov [f], C. Nguyen-Mau [i], D. Orestano [q], F. Pastore [q], L.S. Peak [t], E. Pennacchio [u], H. Pessard [a], R. Petti [h,o], A. Placci [h], G. Polesello [o], D. Pollmann [e], A. Polyarush [l], B. Popov [f,n], C. Poulsen [k], J. Rico [x], P. Riemann [e], C. Roda [h,p], A. Rubbia [h,x], F. Salvatore [o], K. Schahmaneche [n], B. Schmidt [e,h], T. Schmidt [e], A. Sconza [m], M. Sevior [k], D. Sillou [a], F.J.P. Soler [h,t], G. Sozzi [i], D. Steele [b,i], U. Stiegler [h], M. Stipčević [w], Th. Stolarczyk [r], M. Tareb-Reyes [i], G.N. Taylor [k],

0550-3213/01/$ – see front matter
PII: S0550-3213(01)00339-X

RAPID COMMUNICATION

V. Tereshchenko [f], A. Toropin [l], A.-M. Touchard [n], S.N. Tovey [h,k], M.-T. Tran [i], E. Tsesmelis [h], J. Ulrichs [t], L. Vacavant [i], M. Valdata-Nappi [d,y], V. Valuev [f,j], F. Vannucci [n], K.E. Varvell [t], M. Veltri [u], V. Vercesi [o], G. Vidal-Sitjes [h], J.-M. Vieira [i], T. Vinogradova [j], F.V. Weber [c,h], T. Weisse [e], F.F. Wilson [h], L.J. Winton [k], B.D. Yabsley [t], H. Zaccone [r], K. Zuber [e], P. Zuccon [m]

[a] *LAPP, Annecy, France*
[b] *Johns Hopkins University, Baltimore, MD, USA*
[c] *Harvard University, Cambridge, MA, USA*
[d] *University of Calabria and INFN, Cosenza, Italy*
[e] *Dortmund University, Dortmund, Germany*
[f] *JINR, Dubna, Russia*
[g] *University of Florence and INFN, Florence, Italy*
[h] *CERN, Geneva, Switzerland*
[i] *University of Lausanne, Lausanne, Switzerland*
[j] *UCLA, Los Angeles, CA, USA*
[k] *University of Melbourne, Melbourne, Australia*
[l] *Inst. Nucl. Research, INR, Moscow, Russia*
[m] *University of Padova and INFN, Padova, Italy*
[n] *LPNHE, University of Paris VI and VII, Paris, France*
[o] *University of Pavia and INFN, Pavia, Italy*
[p] *University of Pisa and INFN, Pisa, Italy*
[q] *Roma Tre University and INFN, Rome, Italy*
[r] *DAPNIA, CEA Saclay, France*
[s] *University of South Carolina, Columbia, SC, USA*
[t] *University of Sydney, Sydney, Australia*
[u] *University of Urbino, Urbino, and INFN Florence, Italy*
[v] *IFIC, Valencia, Spain*
[w] *Rudjer Bošković Institute, Zagreb, Croatia*
[x] *ETH Zürich, Zürich, Switzerland*
[y] *Now at University of Perugia and INFN, Italy*

Received 19 June 2001; accepted 5 July 2001

Abstract

Results from the ν_τ appearance search in a neutrino beam using the full NOMAD data sample are reported. A new analysis unifies all the hadronic τ decays, significantly improving the overall sensitivity of the experiment to oscillations. The "blind analysis" of all topologies yields no evidence for an oscillation signal. In the two-family oscillation scenario, this sets a 90% CL allowed region in the $\sin^2 2\theta_{\mu\tau}$–Δm^2 plane which includes $\sin^2 2\theta_{\mu\tau} < 3.3 \times 10^{-4}$ at large Δm^2 and $\Delta m^2 < 0.7\ \mathrm{eV}^2/c^4$ at $\sin^2 2\theta_{\mu\tau} = 1$. The corresponding contour in the $\nu_e \to \nu_\tau$ oscillation hypothesis results in $\sin^2 2\theta_{e\tau} < 1.5 \times 10^{-2}$ at large Δm^2 and $\Delta m^2 < 5.9\ \mathrm{eV}^2/c^4$ at $\sin^2 2\theta_{e\tau} = 1$. We also derive limits on effective couplings of the τ lepton to ν_μ or ν_e.

Keywords: Appearance; Neutrino mass; Neutrino oscillations

E-mail address: roberto.petti@cern.ch (R. Petti).

1. Introduction

The NOMAD experiment was designed in 1991 to search for ν_τ appearance from neutrino oscillations in the CERN wide-band neutrino beam produced by the 450 GeV proton synchrotron. Given the neutrino energy spectrum and the distance between the neutrino source and the detector ($\sim$ 600 m on average), the experiment is sensitive to differences of mass squares $\Delta m^2 > 1$ eV^2.

The experiment was motivated by theoretical arguments suggesting that the ν_τ may have a mass of 1 eV, or larger, and therefore could be the main constituent of the dark matter in the universe. This suggestion was based on two assumptions:

- the interpretation of the solar neutrino deficit [1] in terms of $\nu_e \to \nu_\mu$ oscillations amplified by matter effects [2], giving $\Delta m^2 \approx 10^{-5}$ eV^2;
- the so-called "see-saw" model [3] which predicts that neutrino masses are proportional to the square of the mass of the charged lepton, or of the charge $2/3$ quark of the same family.

From these two assumptions one expects a ν_μ mass of $\sim 3 \times 10^{-3}$ eV and a ν_τ mass of ~ 1 eV, or higher. Furthermore, in analogy with quark mixing, neutrino mixing angles were expected to be small.

It is within this theoretical scenario that the NOMAD experiment [4] started a direct search for $\nu_\mu \to \nu_\tau$ oscillations together with another experiment (CHORUS) which used the same neutrino beam but searched for ν_τ appearance with a complementary technique [5].

The detection of an oscillation signal in NOMAD relies on the identification of ν_τ charged–current (CC) interactions using kinematic criteria. The spatial resolution of the detector does not resolve the τ decay vertex from the ν_τ CC interaction. The identification of ν_τ CC events is thus achieved by exploiting all the kinematic constraints which can be constructed from a precise measurement of all visible final-state particles. This requires a detector with good energy and momentum resolution and sophisticated analysis schemes. The NOMAD experiment is the first neutrino oscillation search to use this technique [6].

From 1995 to 1998 the experiment has collected 1040000 events with an identified muon, corresponding to about 1350000 ν_μ CC interactions, given the combined trigger, vertex identification, and muon detection efficiency of 77%.

A recent paper [7] described a search for $\nu_\mu \to \nu_\tau$ and $\nu_e \to \nu_\tau$ oscillations in the full NOMAD data sample. The analysis was based on both deep inelastic (DIS) interactions and low-multiplicity (LM) events for all the accessible τ decay channels. No evidence for oscillations was observed.

In this paper we report an improved ν_τ appearance search in the hadronic τ decay channels. We then combine this search with the analyses of the $\nu_\tau e \bar{\nu}_e$ DIS channel and of the LM topologies described in Ref. [7] and we present the overall NOMAD results. The new analysis unifies all the hadronic τ decay topologies ($\nu_\tau h$, $\nu_\tau \rho$ and $\nu_\tau 3h$) in a single selection scheme. A refined implementation of kinematics, exploiting all the available degrees of freedom, together with new algorithms for the rejection of CC backgrounds

leads to an improvement of the combined NOMAD sensitivity to oscillations by almost a factor of two with respect to Ref. [7]. The systematic uncertainties are also substantially reduced.

2. NOMAD detector

The NOMAD detector (Fig. 1) is described in detail in Ref. [4]. Inside a 0.4 T magnetic field there is an active target consisting of drift chambers (DC) [8] with a fiducial mass of about 2.7 tons and a low average density (0.1 g/cm^3). The target, 405 cm long and corresponding to about one radiation length, is followed by a transition radiation detector (TRD) [9] for electron identification, a preshower detector (PRS), and a high resolution lead-glass electromagnetic calorimeter (ECAL) [10]. A hadron calorimeter (HCAL) and two stations of drift chambers for muon detection are located just after the magnet coil. The detector is designed to identify leptons and to measure muons, pions, electrons and photons with comparable resolutions. Momenta are measured in the DC with a resolution:

$$\frac{\sigma_p}{p} \simeq \frac{0.05}{\sqrt{L\ [\mathrm{m}]}} \oplus \frac{0.008 \times p\ [\mathrm{GeV}/c]}{\sqrt{L\ [\mathrm{m}]^5}},$$

where L is the track length and p is the momentum. The energy of electromagnetic showers, E, is measured in the ECAL with a resolution:

$$\frac{\sigma_E}{E} = 0.01 \oplus \frac{0.032}{\sqrt{E\ [\mathrm{GeV}]}}.$$

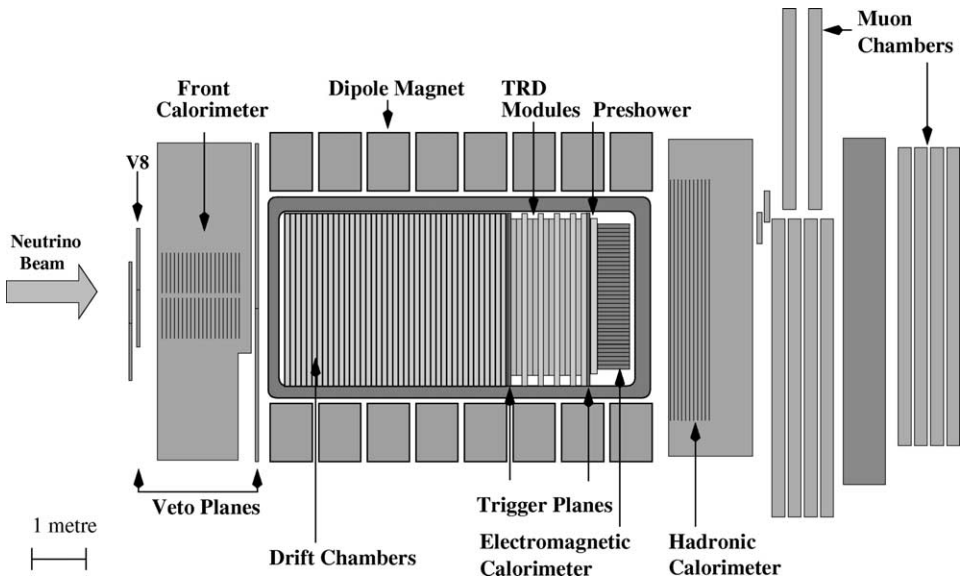

Fig. 1. Side view of the NOMAD detector.

The neutrino interaction trigger [11] consists of a coincidence between signals from two planes of counters located after the active target, in the absence of a signal from a large area veto system in front of the NOMAD detector.

3. Neutrino beam and event samples

From recent beam computations [12], the relative composition of CC events in NOMAD is estimated to be ν_μCC : $\bar{\nu}_\mu$CC : ν_eCC : $\bar{\nu}_e$CC = 1.00 : 0.0227 : 0.0154 : 0.0016, with average neutrino energies of 45.4, 40.8, 57.5, and 51.5 GeV, respectively. The prompt ν_τ component is negligible [13]. Neutrinos are produced at an average distance of 625 m from the detector. Overall, the experiment collected 5×10^{19} protons on tape. In addition to the ν_μ CC events, the data contain about 34000 $\bar{\nu}_\mu$ CC, 21000 ν_e CC, 2300 $\bar{\nu}_e$ CC interactions, and 485000 neutral current (NC) interactions.

Neutrino interactions are simulated using a modified versions of LEPTO 6.1 [14] and JETSET 7.4 [15] with Q^2 and W^2 cutoff parameters removed, and with τ mass and polarization effects included. We use the nucleon Fermi motion distribution of Ref. [16], truncated at 1 GeV/c. To define the parton content of the nucleon for the cross-section calculation we use the GRV-HO parametrization [17] of the parton density functions, available in PDFLIB [18]. A full detector simulation based on GEANT [19] is performed. Further corrections to these samples are applied using the data themselves, as described in Section 4.2. The size of the simulated samples exceeds the data sample by a factor of about 3 for ν_μ CC interactions, 10 for NC and $\bar{\nu}_\mu$ CC interactions and 100 for ν_e and $\bar{\nu}_e$ CC interactions. In addition, more than 500000 ν_τ CC events have been generated for each τ^- decay channel.

4. Analysis principles

From the kinematical point of view, ν_τ CC events in NOMAD are fully characterized by the (undetected) decay of the primary τ. The presence of visible secondary τ decay products, $\tau_{\rm V}$, distinguishes them from NC interactions, whereas the emission of one (two) neutrino(s) in hadronic (leptonic) τ decays provides discrimination against ν_μ (ν_e) CC interactions (Fig. 2). Consequently, in ν_τ CC events the transverse component of the total visible momentum and the variables describing the visible decay products have different absolute values and different correlations with the remaining hadronic system, H, than in ν_μ (ν_e) CC and NC interactions. The optimal separation between signal and background is achieved when all the degrees of freedom of the event kinematics (and their correlations) are exploited.

A rejection power against backgrounds of $\mathcal{O}(10^5)$ is required from the kinematic analysis in order to match the data sample size (Section 3). In addition, the potential ν_τ signal allowed by limits from previous experiments [20,21] is at least by a factor of 0.0025 times smaller than the main ν_μ CC component. Therefore, the ν_τ appearance search in NOMAD is a search for rare events within large background samples. This imposes severe

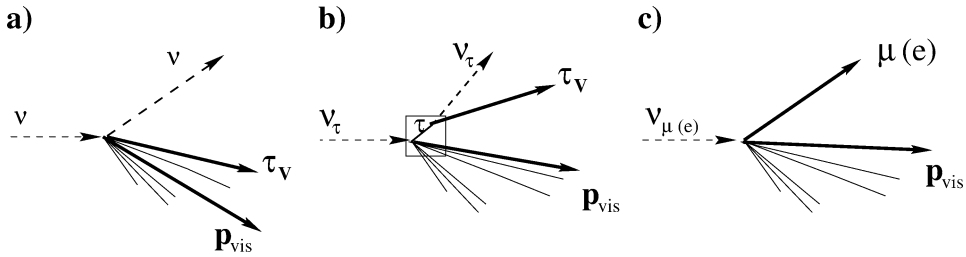

Fig. 2. Signal and background topologies in NOMAD: (a) NC background; (b) ν_τ CC signal with subsequent τ decay; (c) ν_μ (ν_e) CC background. The square indicates the reconstructed "primary" vertex for ν_τ CC interactions. The effect of the τ_V selection on ν_μ (ν_e) CC topologies is discussed in Sections 5.3 and 5.4.

constraints on the analysis techniques. In order to obtain reliable background estimates we have developed methods to correct Monte Carlo (MC) predictions with experimental data and we have defined appropriate control samples to check our predictions.

This paper describes a new search for ν_τ CC interactions in the hadronic τ decay channels $h^-(n\pi^0)\nu_\tau$ and $h^-h^+h^-(n\pi^0)\nu_\tau$, for a total branching ratio of 64.7% [25]. The analysis focuses on DIS events, defined by a cut on the total hadronic momentum recoiling against the visible τ decay product(s), $p^H > 1.5$ GeV/c.

Neutrino interactions in the active target are selected by requiring the presence of at least one charged track in addition to the potential τ decay products, originating from a common vertex in the detector fiducial volume. Quality cuts are then applied to ensure that the selected events are properly reconstructed. This is obtained by imposing constraints on the statistical significance of the main kinematic variables (see Appendix A and Section 5.5): $\sigma(p_T^m)/p_T^m$ (transverse plane), $\sigma(Q_{\rm Lep})/Q_{\rm Lep}$, $\sigma(p^{\tau_V})/p^{\tau_V}$ and $\sigma_{\rm max}(p)/p^{\tau_V}$ ($[\mathbf{p}^{\tau_V}, \mathbf{p}^H]$ plane). In addition, loose requirements based on approximate charge balance at the primary vertex are also applied. Overall, these quality cuts typically remove 10 to 15% of the events.

The separation of ν_τ CC interactions from backgrounds is described in detail in Section 5 and can be summarized in the following steps (Fig. 16):

- the visible τ decay products τ_V are identified on the basis of their topology (Section 5.1);
- constraints are applied to the structure of the hadronic system H recoiling against τ_V (Section 5.2);
- specific algorithms are used to identify and veto primary leptons originating from ν_μ (ν_e) CC interactions (Section 5.3);
- constraints are imposed on the internal structure of the selected τ_V candidate (Section 5.4);
- the final background rejection is achieved by exploiting all the available information from the global event topology (Section 5.5).

Section 6 is devoted to the background estimate, with a description of the data corrections (Section 6.1) and of the control samples used to check background predictions (Section 6.2). Systematic errors are discussed in Section 7. The final results from the

analysis of the hadronic DIS channels are then combined in Section 8 with the remaining topologies from Ref. [7].

In the following we describe the main analysis principles, which have been extensively discussed in Refs. [7,26].

4.1. Statistical analysis of data

The kinematic variables used in the present analysis are defined in Appendix A. In order to exploit their correlations, these variables are combined into likelihood functions. These functions are partial two-, three- or four-dimensional (2D, 3D, 4D) probability density functions (pdf), denoted in the following by square brackets (e.g., $[a, b]$ denotes the 2D correlation between the variables a and b). The final likelihood function, $\mathcal{L}$, is then obtained from a combination of partial pdf's which includes correlations (denoted again by square brackets) among them. This analysis technique provides the best sensitivity to oscillations. As is common practice, the logarithm of the final likelihood ratio between test hypotheses, $\ln\lambda$, is used.

A fit to $\ln\lambda$ with separate signal and background components can increase the statistical power of the search. However, since few events are expected in the signal region, we combine regions of similar signal to background ratio into suitably chosen bins of variable size (Section 5.5). These bins are then treated as statistically independent (Section 8.3).

4.2. Data simulator

In order to reliably compute signal and background efficiencies, the MC results are corrected using the data themselves (Section 6.1). We perform this correction by using a sample of ν_μ CC events from the data, removing the *identified* muon, and replacing it with a MC-generated lepton ℓ of appropriate momentum vector, where ℓ can be a ν, an e^- or a τ^- followed by its decay. In addition, as explained in Section 6.1, events with identified muons or electrons are directly used to correct CC background predictions in the hadronic τ decays. All these samples are referred to as the Data Simulator (DS).

The same procedure is then applied to reconstructed MC ν_μ CC events and these event samples are referred to as the Monte Carlo Simulator (MCS). In order to reduce systematic uncertainties, signal and background efficiencies ϵ are then obtained from the relation:

$$\epsilon = \epsilon_{\mathrm{MC}} \times \epsilon_{\mathrm{DS}}/\epsilon_{\mathrm{MCS}},$$

which implies that efficiencies for lepton reconstruction are obtained from the MC (ϵ_{MC}), while the effect of the hadronic jet differences between data and simulations is taken into account through the ratio $\epsilon_{\mathrm{DS}}/\epsilon_{\mathrm{MCS}}$. It has been checked that efficiencies obtained by this method are indeed stable with respect to variations of the MC input models (nuclear effects, fragmentation, Fermi motion, detector resolution functions) within the quoted uncertainty.

The errors on background predictions given in all the following tables reflect the statistical uncertainties from MC, MCS and DS. Systematic uncertainties are discussed in Section 7.

4.3. Avoiding biases

A procedure referred to as "blind analysis" is used. According to this procedure, data events inside the signal region (the "blind box") cannot be analyzed until all the selection criteria are defined and the robustness of the background predictions is demonstrated with appropriate control samples (Section 6.2). The selection criteria are chosen by optimizing the sensitivity to oscillations (Section 5.5). This is defined as the average upper limit on the oscillation probability that would be obtained, in the absence of a signal, by an ensemble of experiments with the same expected background [27].

The sensitivity to oscillations also provides the final criterion for any choice between different analyses of the same τ decay topology or for the replacement of a previous analysis by a newer one. The choice is made before looking at data events falling in the signal region.

The MC samples used to define the selection criteria are different from those used to evaluate the background and signal efficiency, which are therefore fully unbiased.

5. Selection scheme

The new selection of hadronic τ decays unifies four specific decay topologies in a single general scheme:

- 0γ: $\tau \to \nu_\tau \pi$ decays. The τ_V candidate is built from a single charged track.
- 1γ: $\tau \to \nu_\tau \rho \to \nu_\tau \pi \pi^0$ decays where the π^0 is reconstructed as a single ECAL cluster either because the two photons overlap in ECAL or because one of them is not reconstructed in ECAL. The τ_V candidate is built from a charged track and from a single ECAL neutral cluster.
- 2γ: $\tau \to \nu_\tau \rho \to \nu_\tau \pi \pi^0$ decays where the π^0 is reconstructed from two separate ECAL clusters. The τ_V candidate is built from a charged track and from two ECAL neutral clusters.
- $3h$: $\tau \to \nu_\tau a_1 \to \nu_\tau \pi \rho^0 \to \nu_\tau \pi \pi \pi$ decays. The τ_V candidate is built from three charged tracks.

Each topology is independently analyzed with the *same selection criteria*. Events selected by more than one topology define a further sample. Eventually, we combine the different topologies into a single search. This statistical treatment provides the best overall sensitivity to oscillations. Photon conversions in the DC volume are not used for π^0 reconstruction in this analysis. However, events where only one of the γ's from π^0 decay converts into an e^+e^- pair are included in the 1γ topology. The signal efficiencies quoted in the following refer to the $\nu_\tau h(n\pi^0)$ (Br 49.5%) or $\nu_\tau 3h(n\pi^0)$ (Br 15.2%) [25] inclusive DIS samples.

The selection scheme is intended to exploit, at each step, all the available topological information (degrees of freedom) through the use of appropriate probability density functions based on correlations among kinematic variables. As explained in Appendix A,

an event in NOMAD can be fully described by five degrees of freedom (Fig. 16): three in the transverse plane (x, y) and two along the beam direction (z).

5.1. Identification of τ decay product(s)

In hadronic τ decays the selection of the visible decay product(s) relies on topological constraints. This implies that, for a *given event*, more than one choice is possible and therefore a discriminating criterion is needed. Since the total visible momentum of the event ($E_{\rm vis}$ and p_T^m) is fixed in the problem, only three degrees of freedom related to the general event structure are available. In addition, when applicable, the internal structures of $\tau_{\rm V}$ and H provide further constraints.

A single likelihood function, $\mathcal{L}^{\rm S}$, is used to select among all the combinations the most likely $\tau_{\rm V}$ originating from a τ decay:

$$\mathcal{L}^{\rm S} \equiv \left[\left(\mathcal{L}^{\rm IN}\right), R_{Q_T}, y_{Bj}, \theta_{\tau_{\rm V}H}\right].$$

The 2D correlations between the three variables R_{Q_T}, y_{Bj} and $\theta_{\tau_{\rm V}H}$ (Appendix A) are shown in Fig. 3 (left plots). The function $\mathcal{L}^{\rm IN}$ describes the internal $\tau_{\rm V}$ structure for the 1γ, 2γ and $3h$ topologies (obviously, it cannot be defined for the 0γ topology):

$$\mathcal{L}^{\rm IN} \equiv \begin{cases} [M_\rho, \theta_{\pi^-\pi^0}, E_{\pi^0}/E_{\rm vis}], & 1\gamma, \\ \left[[M_{\pi^0}, \theta_{\gamma\gamma}, E_\gamma^{\max}/E_{\rm vis}], M_\rho, \theta_{\pi^-\pi^0}, E_{\pi^0}/E_{\rm vis}\right], & 2\gamma, \\ \left[\left[\overline{M}_{\rho^0}, \bar{\theta}_{\pi^+\pi^-}, E_{\pi^+}\right], M_{a_1}, \theta_{\pi^-\pi^-}, \overline{E}_{\rho^0}\right], & 3h, \end{cases}$$

where, for the $3h$ topology, the average of the two indistinguishable $\pi^+\pi^-$ combinations $(\overline{M}_{\rho^0}, \bar{\theta}_{\pi^+\pi^-}, \overline{E}_{\rho^0})$ is used. This function is based on the decay kinematics of the ρ (1γ and 2γ) and a_1 ($3h$) resonances in the laboratory frame. In the definition of $\mathcal{L}^{\rm IN}$ the invariant masses are considered as free parameters.

The isolation variable R_{Q_T} is sensitive to the internal structure of the hadronic system and thus incorporates additional information with respect to the degrees of freedom related to the global event topology. The use of this variable for the $\tau_{\rm V}$ identification results, overall, in four degrees of freedom in addition to the $\tau_{\rm V}$ internal structure. However, only three of them are physically relevant for the $\tau_{\rm V}$ identification and are therefore included in $\mathcal{L}^{\rm S}$. This procedure (and the choice of the variables entering $\mathcal{L}^{\rm S}$) also minimizes potential biases induced on background events, in which a fake (not coming from τ decay) $\tau_{\rm V}$ is indeed constructed by the $\tau_{\rm V}$ identification algorithm itself.

A likelihood ratio, $\ln\lambda^{\rm S}$, is built as the ratio of the $\mathcal{L}^{\rm S}$ function for correct and wrong combinations of τ decay products in ν_τ CC events. In each event, the system of particles with maximum $\ln\lambda^{\rm S}$ among all possible combinations is tagged as $\tau_{\rm V}$. No cut is applied on $\ln\lambda^{\rm S}$, which is constructed from *signal events* only and, therefore, is not the optimal discriminant against backgrounds (Section 5.4). After the $\tau_{\rm V}$ identification, a minimum γ energy of 200 MeV (100 MeV) is required for the 1γ (2γ) topology in order to remove fake photons. The algorithm correctly identifies the visible τ decay product(s) in 91%, 80%, 80% and 73% of all the 0γ, 1γ, 2γ and $3h$ ν_τ CC events, respectively. These values set an approximate upper limit to the final selection efficiency, since events with a mis-identified $\tau_{\rm V}$ do not have the kinematics expected from ν_τ CC events (Section 5.5).

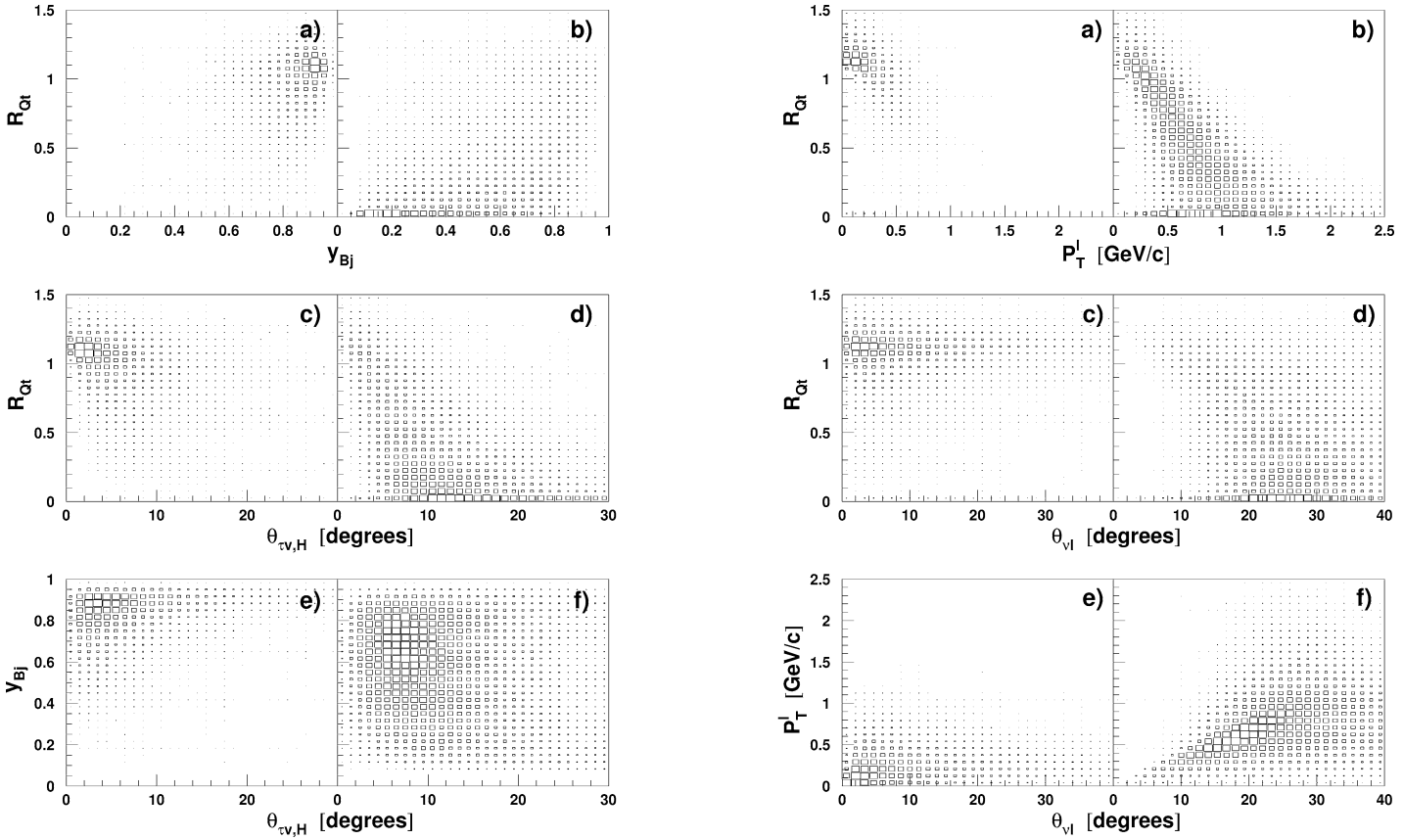

Fig. 3. Left plots: correlations between kinematic variables, not related to the internal τ_V structure, used to construct $\ln\lambda^S$ for wrong (a, c, e) and correct (b, d, f) combinations of τ decay products in $\nu_\tau\pi$ decays (Section 5.1). Right plots: correlations between kinematic variables used to construct $\ln\lambda^V$ for wrong tracks (a, c, e) and for the true leading muon (b, d, f) in ν_μ CC events passing the first level veto (Section 5.3).

5.2. Structure of the H system

For background events the τ_V candidate is mostly selected inside the hadronic jet. In NC interactions the whole visible event is indeed a hadronic jet (Fig. 2a). On the other hand, in CC interactions where the leading lepton is not identified and the τ_V particle(s) are embedded in the jet, the remaining hadronic system H has an incorrect topology (Fig. 4b). As a consequence, a constraint on the structure of the hadronic system significantly increases the background rejection.

In order to effectively reject both NC and CC topologies, the jet structure must include information from τ_V. This is achieved by defining the variable:

$$S_H \equiv \frac{\langle Q_T^2 \rangle_H}{\Delta r_{\tau_V h_i}^{2/3}},$$

which takes into account the transverse size of the hadronic system, $\langle Q_T^2 \rangle_H$, and the opening of the minimum invariant cone between τ_V and any other charged track, $\Delta r_{\tau_V h_i}$. The requirement $S_H < 0.20$ (0.16) GeV$^2/c^2$ in the one (three) prong search selects dijet topologies. Due to the higher average multiplicity, the $3h$ topology is more sensitive to variables related to the internal structure of τ_V (Section 5.4) and H, thus requiring a tighter constraint.

An additional check of the H structure is obtained by removing τ_V and by computing the maximum transverse momentum Q_{Lep} among all charged tracks within the hadronic system. As explained in Section 5.3.2, events originating from ν_e ($\bar{\nu}_e$) CC interactions are indeed characterized by large values of Q_{Lep} for the *leading lepton*. The condition $Q_{\text{Lep}}^{\max} < 5.0$ GeV/c further suppresses topologies where the unidentified leading electron (positron) is erroneously included in the hadronic system (Fig. 4b).

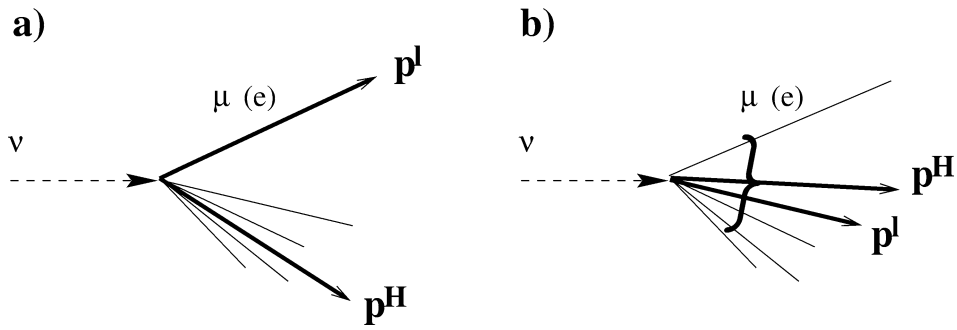

Fig. 4. Possible topologies for an unidentified ν_μ (ν_e) CC interaction after the selection of a leading charged track in the analysis: (a) the primary lepton is chosen as the leading particle; (b) the primary lepton is included in the hadronic system H. Similar considerations can be applied to the τ_V selection (l is replaced by τ_V). However, for the 1γ, 2γ and $3h$ samples the choice of the primary lepton as one of the τ_V particles can produce additional topologies, as explained in Section 5.4 and shown in Fig. 5.

5.3. Lepton veto

Due to the presence of a highly isolated track (leading lepton), *unidentified* CC interactions can fake hadronic τ decays. As discussed above, the selection of a single leading charged track defines two different topologies in CC background events, depending on whether the leading lepton is the chosen track (Fig. 4a) or is included in the remaining hadronic system H (Fig. 4b). In the latter case the transverse plane kinematics is significantly distorted by the selection of a random leading particle, thus reducing their effectiveness. Specific algorithms are then developed in order to tag the leading lepton. The selection can be divided in two steps:

- *First level veto* (FLV). Lepton identification criteria are used to reject events containing clear primary leptons of any charge.
- *Second level veto* (SLV). A kinematic criterion based on event topology is used to tag a *single* lepton candidate, l^{μ}_{CC} or l^{e}_{CC}, among all negatively charged primary tracks. Subsequently, additional lepton identification criteria are imposed to the selected track.

This method aims at avoiding tight lepton identification criteria. In particular, it is also possible to analyze events outside the geometrical acceptance of the relevant subdetectors (Fig. 1). The analyses described in Ref. [7] were instead based on tight identification conditions and rejected all events containing high p_T tracks escaping the detector. This resulted in a significant efficiency loss. The kinematic tagging plays a crucial role in the veto algorithm because events in which the leading lepton is correctly tagged are efficiently rejected by kinematics (Section 5.5).

5.3.1. Muon tagging and veto

The FLV rejects events containing a μ^- (μ^+) positively identified by the reconstruction algorithms or by the presence of residual hits and track segments associated to a charged track in both stations of the muon chambers.

The muon tagging in the SLV is based on the likelihood function:

$$\mathcal{L}^{\mathrm{V}} \equiv \left[R_{Q_T}, p_T^l, \theta_{\nu l}\right],$$

which is similar to $\mathcal{L}^{\mathrm{S}}$ but takes into account the topology of ν_μ CC interactions with unidentified muons. These events are characterized, in general, by large values of y_{Bj}, and the effect of variables relating the hadronic system to the muon track is weaker. For this reason, $\mathcal{L}^{\mathrm{V}}$ only includes variables directly describing properties of the track being considered. The 2D correlations between variables used to construct $\mathcal{L}^{\mathrm{V}}$ are shown in Fig. 3 (right plots).

A likelihood ratio, $\ln\lambda^{\mathrm{V}}$, is built from ν_μ CC events *surviving the FLV*, as the ratio of $\mathcal{L}^{\mathrm{V}}$ for the true muon and for other tracks. In the three prong search l^{μ}_{CC} is defined as the track with maximum $\ln\lambda^{\mathrm{V}}$ among all the negatively charged primary tracks. In the one prong search the tagging efficiency can be further increased by considering the bias induced by the τ_{V} selection, which returns a single charged track. In this case the τ_{V} charged track is

also tagged as l^{μ}_{CC} if, for this track, $\ln\lambda^{\mathrm{V}} > 0$, otherwise l^{μ}_{CC} is chosen as the track with maximum $\ln\lambda^{\mathrm{V}}$ (the most likely muon).

The algorithm correctly identifies the true muon in 94%, 89%, 89% and 86% of ν_μ CC surviving the FLV for the 0γ, 1γ, 2γ and $3h$ topologies. In addition, the muons not identified by the algorithm have very low energy and are thus generally included in the hadronic system H (Fig. 4b). This results in a NC-like configuration which is efficiently rejected by kinematics against NC interactions (Section 5.5).

Only events in which l^{μ}_{CC} is compatible with being a minimum ionizing particle in both ECAL and HCAL are rejected at this stage. The suppression of the remaining ν_μ CC background is achieved by exploiting the complete event kinematics under the assumption that l^{μ}_{CC} *is the leading particle* (see Appendix A), as explained in Section 5.5.

5.3.2. Electron veto

Although ν_e ($\bar{\nu}_e$) CC events represent only a tiny fraction of the full neutrino interactions (Section 3), ν_e ($\bar{\nu}_e$) can be potentially more dangerous than ν_μ CC events. This is due to the lower identification efficiency of electrons with respect to muons (limited angular acceptance of TRD, efficiency loss for π rejection, bremsstrahlung emission, etc.) and to the fact that this effect is not restricted to specific topologies. In addition, ν_e have a harder energy spectrum, because they originate mainly from K decays, and therefore the primary lepton is well isolated from the hadronic jet. However, in the hadronic τ decays the presence of γ's from π^0 (sometimes converting in the DC volume) can produce electron-like signals. For this reason, the analysis does not use stringent constraints against ν_e ($\bar{\nu}_e$) CC interactions, which would result in a significant loss of efficiency.

The FLV is designed to reject two different classes of events. First, events containing a primary track which is *positively identified* as e^- (e^+) by both TRD and loose PRS requirements are rejected if, for this track, $p^l_T/p^m_T > 1.0$ and $p^l_T > 1.0$ GeV/c. These are mainly high p_T e^- (e^+) in events with small missing transverse momentum. A second background source originates from ν_e ($\bar{\nu}_e$) CC interactions where *no particle identification* is available because the primary electron (positron) emitted most of its energy as a hard bremsstrahlung γ and missed the relevant subdetectors. Therefore, for each primary track (of either charge) not reaching the TRD, we search for potential bremsstrahlung secondaries with direction tangential to the track. The presence of such additional γ's or charged particles is then used as a kind of "electron tag" and the event is rejected if, for the fully reconstructed lepton (sum of primary track and bremsstrahlung secondaries), $p^l_T/p^m_T > 1.5$ and $p^l_T > 1.0$ GeV/c.

Since, contrary to the muon case, the electron identification inefficiencies are not restricted to specific topologies, the SLV tagging criterion is simply based on $\ln\lambda^{\mathrm{S}}$. A l^{e}_{CC} candidate is then defined as the τ_{V} charged track in one-prong events and as the negative τ_{V} track with the larger momentum uncertainty in three-prong events. Events from ν_e CC interactions in which the primary electron is chosen as τ daughter candidate are indeed dangerous because they are highly isolated and cannot be suppressed by studying the jet structure. This happens in 85%, 62%, 57% and 51% of all ν_e CC events for the 0γ, 1γ,

2γ and $3h$ topologies. These events are rejected if the l^e_{CC} track fulfills loose electron identification criteria based on TRD and on the combined PRS-ECAL information.

As described in the following, the background in the most sensitive region of the analysis (Table 5) consists almost entirely of ν_e ($\bar{\nu}_e$) CC interactions. This is partially explained by the kinematic approach used (Section 5.5).

5.4. Structure of the τ_V candidate

For the 1γ, 2γ and $3h$ topologies the internal τ_V structure provides further discrimination against backgrounds. The corresponding information, incorporated into the $\mathcal{L}^{IN}$ function, has been already used for the τ_V identification (Section 5.1), through the likelihood ratio between correct and random combinations *in signal events.*

Once the τ_V selection is performed, background events can still have a τ_V internal structure inconsistent with τ decay. In particular, the CC sample contains two specific topologies. The first one includes events where τ_V consists of the leading μ (e) and of additional particle(s) from the hadronic jet (Fig. 5a). A second possibility arises when the leading electron from a ν_e CC interaction undergoes hard bremsstrahlung radiation and τ_V consists of different pieces of the original electron (Fig. 5b). Both cases can be suppressed by a constraint on the τ_V internal structure, which makes use of the presence of ρ or a_1 resonances in τ decays. However, the τ_V internal structure is expected to be less effective against NC background because these events may contain genuine resonances inside the hadronic jet.

A likelihood ratio, $\ln\lambda^{IN}$, is then built as the ratio of the $\mathcal{L}^{IN}$ function between the true combination in signal events and the selected τ_V in a weighted mixture of ν_μ and ν_e CC interactions. A loose cut at $\ln\lambda^{IN} > 0.5, 0.0, 0.0$ is applied for the 1γ, 2γ and $3h$ topologies respectively. The higher charged multiplicity of the $3h$ topology partially correlates the τ_V internal structure to the jet structure (Section 5.2) for backgrounds and therefore a further binning is used along $\ln\lambda^{IN}$ in this case (Section 5.5). Since no kinematic constraint on any variable related to the τ_V structure has been previously imposed, the $\ln\lambda^{IN}$ cut results in a significant event reduction for all samples (Table 1). However, this is due mainly to the

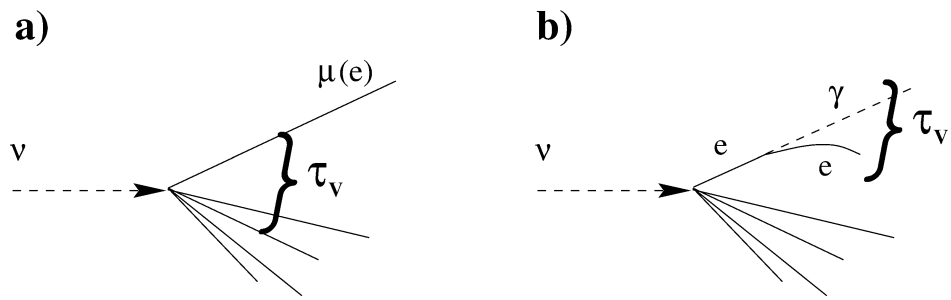

Fig. 5. Internal τ_V topologies (1γ, 2γ and $3h$) for CC backgrounds in which the leading lepton is part of the τ_V candidate: (a) ν_μ (ν_e) CC interaction with part of τ_V embedded in the hadronic jet; (b) ν_e CC interaction with bremsstrahlung emission.

Table 1
Number of observed events and expected background as a function of cuts for all the hadronic DIS decay modes. The corresponding signal efficiency (%) is listed in the first column (ν_τ CC). The effect of the selection on the τ^+ control sample is also shown. The numbers are fully corrected with the data simulator and the last column shows the ratio between data and predicted background. The efficiencies refer to the inclusive $h(n\pi^0)$ and $3h(n\pi^0)$ samples and do not include branching ratios. Overlap events are included in each topology

Sample		ν_τ CC	NC		$\nu_\mu + \bar{\nu}_\mu$ CC		$\nu_e + \bar{\nu}_e$ CC		Tot Bkgnd		Data		Data/Bkgnd	
charge		−	−	+	−	+	−	+	−	+	−	+	−	+
τ_V candidate	0γ	43.7	80739	88663	27532	30852	1612	1426	109883	120941	114012	125013	1.04	1.03
	1γ	43.1	95869	103264	25531	29094	1670	1591	123070	133949	126128	137516	1.02	1.03
	2γ	33.7	79934	80613	21247	25742	1358	1494	102539	107849	105399	109285	1.03	1.01
	$3h$	44.4	105524	116237	37874	41406	1612	2452	145060	160095	148420	165094	1.02	1.03
H structure	0γ	36.3	68383	78517	23987	23420	1305	940	93675	102877	96020	105938	1.02	1.03
	1γ	36.5	81682	90164	20347	22476	1233	1002	103262	113642	104609	115531	1.01	1.02
	2γ	27.7	66257	68570	16533	19187	976	917	83766	88674	85102	89317	1.02	1.01
	$3h$	32.8	88472	98737	28794	31171	1179	1576	118445	131484	116106	134205	0.98	1.02
Lepton veto	0γ	23.7	39319	40077	7422	16299	165	389	46906	56765	47673	54986	1.02	0.97
	1γ	17.5	32128	32260	3930	5598	164	289	36222	38147	36818	39066	1.02	1.02
	2γ	12.6	23569	22800	2847	4345	120	244	26536	27389	27158	27913	1.02	1.02
	$3h$	13.2	19701	25712	2196	2566	182	381	22079	28659	21929	27889	0.99	0.97
$\ln\lambda^{IN}$ cut	0γ	–	–	–	–	–	–	–	–	–	–	–	–	–
	1γ	9.5	8568	7888	718	1499	69	125	9355	9512	9212	9408	0.98	0.99
	2γ	7.1	8702	8048	843	1515	59	113	9604	9676	9840	9951	1.02	1.03
	$3h$	4.9	2411	2366	147	219	28	45	2586	2630	2666	2684	1.03	1.02
$\ln\lambda^{CC}$ cut	0γ	9.7	12020	11464	717	684	55	88	12792	12236	13471	12101	1.05	0.99
	1γ	8.6	7816	7459	565	1127	62	107	8443	8693	8345	8696	0.99	1.00
	2γ	6.2	7864	7509	616	1137	51	95	8531	8741	8789	9097	1.03	1.04
	$3h$	4.2	2079	2025	119	173	20	43	2219	2241	2253	2243	1.02	1.00
$\ln\lambda^{NC}$ cut	0γ	1.3	6.7±2.1	7.3±2.5	0.4±0.4	2.0±0.6	0.7±0.1	4.0±0.3	7.8±2.2	13.3±2.6	10	11	1.28±0.54	0.83±0.30
	1γ	1.4	6.7±2.1	8.9±3.1	0.5±0.4	3.5±0.9	0.9±0.1	4.6±0.4	8.1±2.2	17.0±3.2	8	17	0.99±0.44	1.00±0.31
	2γ	0.8	3.4±1.3	7.9±1.7	1.1±0.6	3.4±0.9	0.9±0.2	3.3±0.4	5.4±1.5	14.6±2.0	6	16	1.11±0.55	1.10±0.31
	$3h$	1.3	2.8±1.4	5.3±1.2	1.5±0.6	2.6±0.9	0.6±0.2	2.0±0.3	4.9±1.5	9.9±1.6	3	10	0.61±0.40	1.01±0.36

rejection of events which *do not contain* τ_V candidates compatible with being a genuine ρ or a_1 resonance.

5.5. Global kinematics

Background events can be divided into two categories with opposite kinematic configurations. In NC interactions *the* τ_V *candidate* is embedded in the hadron jet (Fig. 2a), and a large missing transverse momentum associated with the escaping neutrino is almost opposite to the direction of the hadronic system. On the other hand, *the leading lepton* in CC interactions is typically well-isolated and balances the momentum of the remaining hadronic system in the transverse plane (Fig. 2c). The signal from hadronic τ decays has intermediate properties between these two extremes; the τ decay neutrino introduces a modest amount of missing transverse momentum and the non-colinearity of τ and τ_V can reduce the isolation of τ_V (Fig. 2b).

In order to optimize separately the rejection of each of the two opposite background sources, we implement an event classification based on the use of two distinct likelihood functions. As discussed in the following, this procedure provides the best description of the kinematic information and, at the same time, the possibility to distinguish further between NC and CC backgrounds. The first likelihood function is designed to separate the signal from NC interactions:

$$\mathcal{L}^{\mathrm{NC}} \equiv \left[[[\theta_{\nu T}, \theta_{\nu H}], \theta_{\tau_V h_i}, Q_T], p_T^m, p_T^H\right],$$

where the minimum opening angle $\theta_{\tau_V h_i}$ is sensitive to the internal structure of the hadronic system. Fig. 6 (left plots) illustrates the discriminating power of some correlations between the kinematic variables used to construct $\mathcal{L}^{\mathrm{NC}}$. For each event, a likelihood ratio $\ln\lambda^{\mathrm{NC}}$ is computed as the ratio of the $\mathcal{L}^{\mathrm{NC}}$ functions constructed from the true τ_V combination in signal events and from the selected τ_V combination in NC events, respectively. Since $\mathcal{L}^{\mathrm{NC}}$ is built by selecting τ_V *as the leading particle*, for the CC background a cut on $\ln\lambda^{\mathrm{NC}}$ suppresses the topology where the unidentified lepton has little energy and is part of the hadronic system H (NC-like configuration in Fig. 7). As explained in Section 5.3.1, this reduces the mistagging probability of muons to a negligible level in the final signal region.

The second function is designed to distinguish signal from CC events and is optimized, in particular, to reject ν_μ CC interactions:

$$\mathcal{L}^{\mathrm{CC}} \equiv \left[[R_{Q_T}, R_{p_T}, \theta_{vl}], E_{\mathrm{vis}}, p_T^m, M_T\right],$$

where the first part is similar to the function used for the muon tagging procedure (Section 5.3.1). The function $\mathcal{L}^{\mathrm{CC}}$ uses variables referring to *the tagged muon* l^μ_{CC}

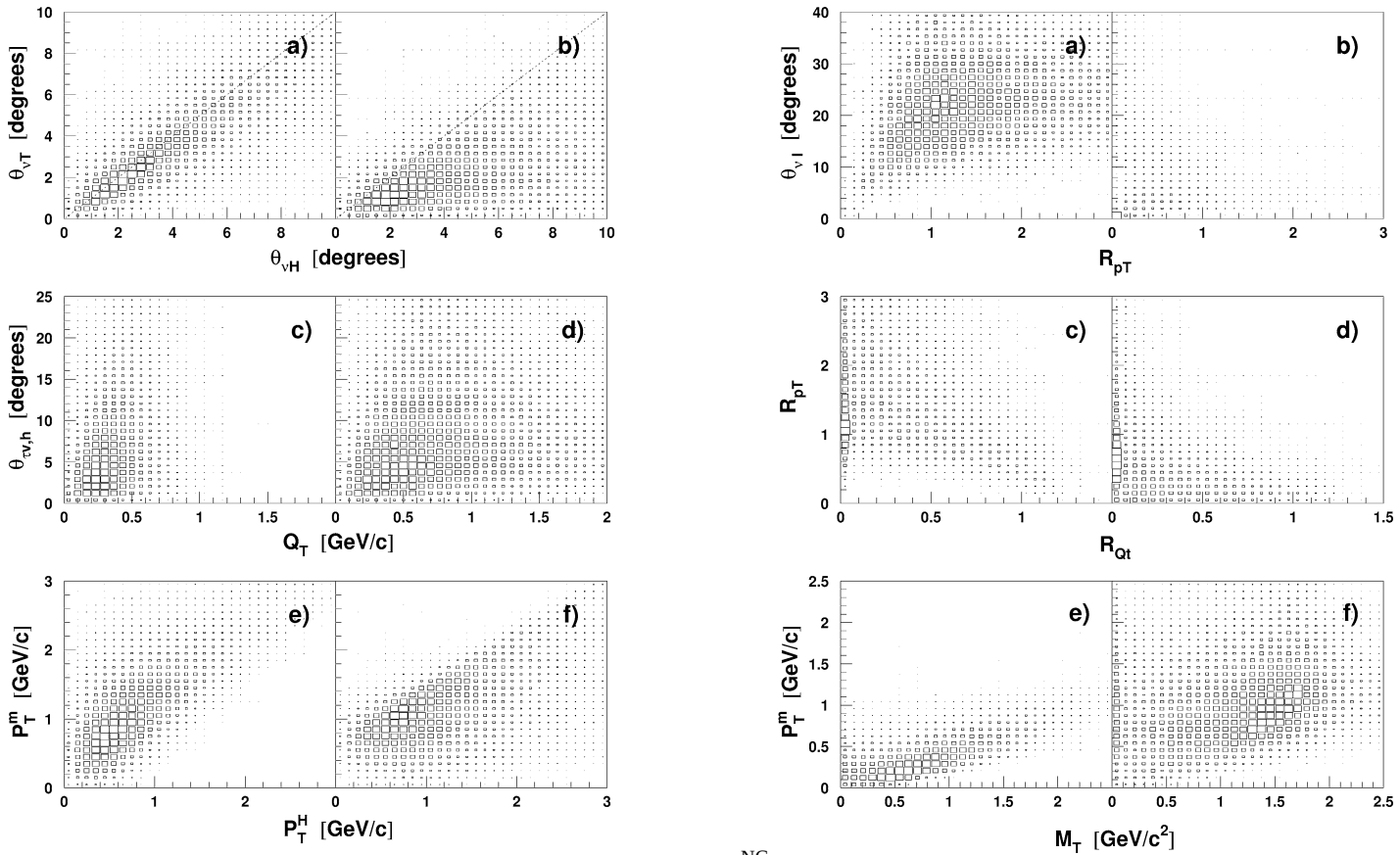

Fig. 6. Left plots: correlations between kinematic variables used to construct $\ln\lambda^{\mathrm{NC}}$ for MC events of type ν_μ NC (a, c, e) and $\tau \to \nu_\tau\pi$ decays with the selection of the right π as leading particle (b, d, f). Right plots: correlations between kinematic variables for MC events of type ν_μ CC with unidentified μ (a, c, e) and $\tau \to \nu_\tau\pi$ decays with the chosen l^{μ}_{CC} as leading particle (b, d, f).

and therefore, for events where the lepton is correctly tagged, it represents the actual CC kinematics (Fig. 4). The potentially different choice of leading particle(s) provides, globally, four additional degrees of freedom (including the R_{Q_T} variable) as explained in Section 5.1, and thus further justifies the use of two distinct likelihood functions. The correlations between some kinematic variables included in $\mathcal{L}^{\mathrm{CC}}$ are shown in Fig. 6 (right plots). For each event, a likelihood ratio $\ln\lambda^{\mathrm{CC}}$ is computed as the ratio of the $\mathcal{L}^{\mathrm{CC}}$ functions constructed from the selected l^{μ}_{CC} in signal events and from the true muon in MC ν_μ CC interactions passing the FLV.

Events are plotted in the plane $[\ln\lambda^{\mathrm{NC}}, \ln\lambda^{\mathrm{CC}}]$, as shown in Fig. 7 for simulated signal (0γ) and backgrounds. Two distinct populations, corresponding to the NC and CC backgrounds, are clearly visible, demonstrating that indeed the two background sources are independent and have opposite overall kinematics. The signal region (the blind box), further subdivided into different bins, lies at large values of both likelihood ratios. This corresponds to the selection of events where the τ_{V} candidate is isolated from the hadronic system and is not fully balanced in the transverse plane.

For all topologies the analysis reaches its optimal sensitivity at low background levels (Table 5). This is an indication that the kinematic rejection of background is optimal. The sensitivity curves of Fig. 8 clearly show a fast rise after the minimum at large values of the likelihood ratios, associated to regions of decreasing signal efficiency and almost background-free. The preliminary quality cuts on the statistical significance of the main variables (Section 4) allows us to exploit such extreme values of the likelihood ratios. Due to the efficient kinematic suppression of the main background sources (NC and ν_μ CC), the very small residual background in these regions consists almost entirely of ν_e ($\bar{\nu}_e$) CC events.

The choice of the binning for the signal region is performed *before* analyzing data events and is the one providing the best overall sensitivity to oscillations (Fig. 8). This criterion allows an objective definition of bins. First, the highest bin is chosen such that its lower edge is as close as possible to the minimum of the curves of Fig. 8, while consistent with a background of less than 0.5 events. Additional bins are then included in the signal region, up to the point where no further significant improvement of the combined sensitivity is obtained. The final binning follows the scheme of Fig. 7 for 0γ and 1γ events. In the 2γ topology, due to the limited statistics, only $\ln\lambda^{\mathrm{NC}}$ is used to define the binning. For

Fig. 7. [On next page, top] Scatter plot of $\ln\lambda^{\mathrm{CC}}$ vs $\ln\lambda^{\mathrm{NC}}$ for MC backgrounds from ν_μ NC (left plot) and ν_μ CC interactions passing the first level veto (middle plot) and simulated $\tau \to \nu_\tau\pi$ (0γ) decays (right plot). The local bin densities are shown in logarithmic scale. The large box at the upper right corner, divided into four bins, defines the signal region, whereas the dotted lines show the control regions used to estimate the systematic uncertainties on CC (region A) and NC (region B) events.

Fig. 8. [On next page, bottom] Definition of the signal region: sensitivity as a function of $\ln\lambda^{\mathrm{NC}}$ for the 0γ, 1γ, 2γ and $3h$ (from left to right) topologies. The vertical lines correspond to the binning used in the analysis. The blind region starts at $\ln\lambda^{\mathrm{NC}} > 5.5, 6.0, 5.5, 4.0$ for the 0γ, 1γ, 2γ and $3h$ topologies, respectively (left vertical lines in each plot). A cut $\ln\lambda^{\mathrm{CC}} > 3.5, 0.0, 0.0, 0.0$ is applied.

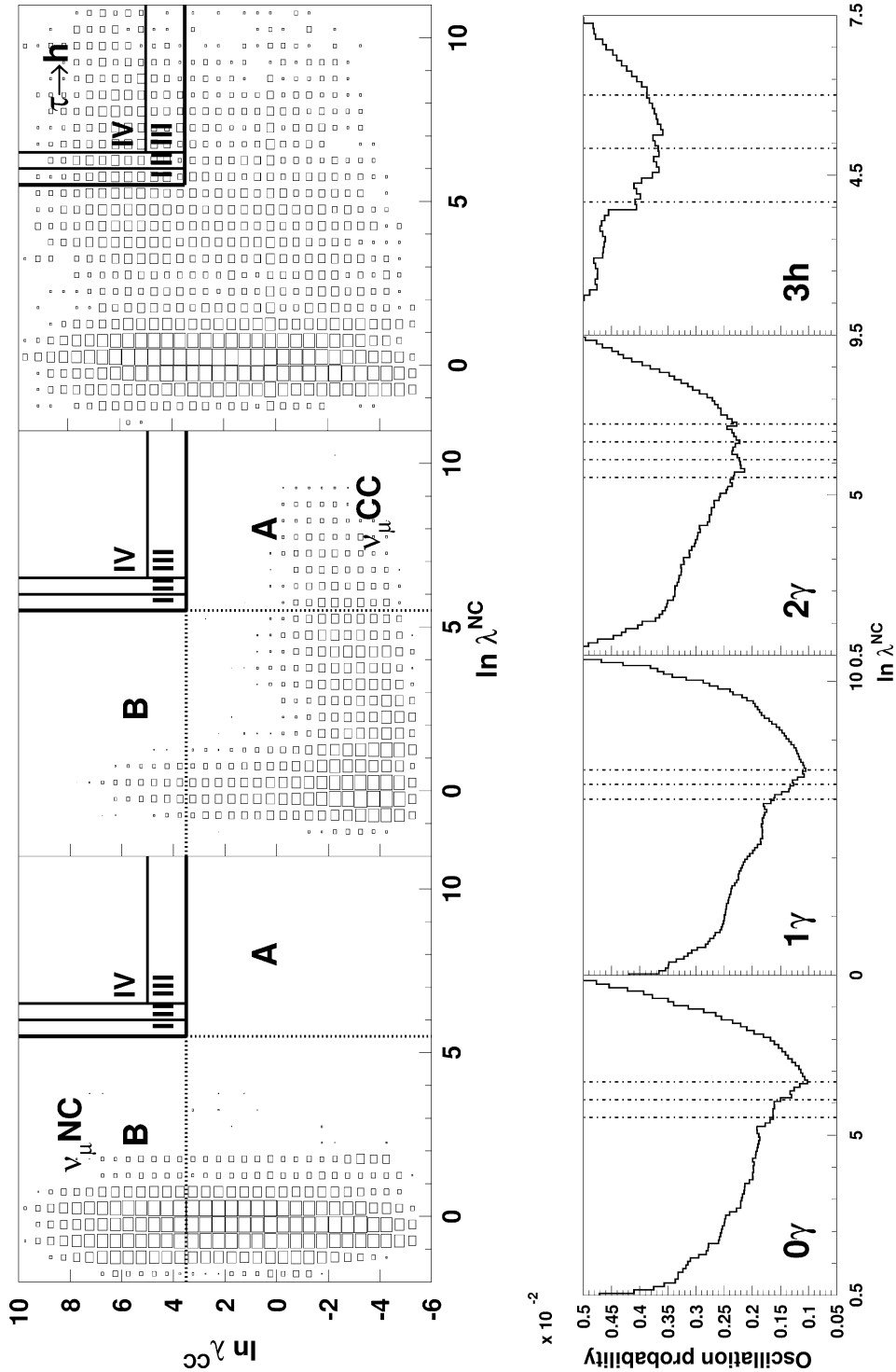
ν_μ NC
ν_μ CC
$\tau \rightarrow h$
A
B
III
IV
$\ln \lambda^{cc}$
$\ln \lambda^{NC}$
Oscillation probability
x 10^{-2}
0γ
1γ
2γ
3h

Table 2
Number of background and data events in the signal region. The corresponding $N_\tau^{\mu\tau}$ and $N_\tau^{e\tau}$, as defined in Sections 7.2 and 8.3, are listed in the last two columns. The $1/2\gamma$ and $0/1$–2γ topologies contain overlap events. The bins denoted by a star are considered as low background bins (Section 8.2)

Analysis			Bin #	Tot Bkgnd	Data	$N_\tau^{\mu\tau}$	$N_\tau^{e\tau}$	
$\nu_\tau h(n\pi^0)$	DIS	0γ	I	4.49 ± 1.50	5	454	10.4	
		0γ	II	3.07 ± 1.17	5	345	8.2	
		0γ	III	$0.05^{+0.60}_{-0.03}$	0	288	6.9	$*$
		0γ	IV	$0.12^{+0.60}_{-0.05}$	0	1345	31.1	$*$
		1γ	I	4.47 ± 1.58	5	283	6.8	
		1γ	II	1.54 ± 0.89	0	244	5.7	
		1γ	III	$0.07^{+0.70}_{-0.04}$	0	223	5.7	$*$
		1γ	IV	$0.07^{+0.70}_{-0.04}$	0	1113	26.6	$*$
		2γ	I	2.57 ± 0.91	3	318	7.4	
		2γ	II	0.66 ± 0.44	0	175	4.1	
		2γ	III	0.49 ± 0.40	0	82	1.9	
		2γ	IV	$0.11^{+0.60}_{-0.06}$	0	211	4.9	$*$
		$1/2\gamma$	I	1.40 ± 0.77	2	154	3.7	
		$1/2\gamma$	II	$0.17^{+0.70}_{-0.08}$	0	124	2.9	
		$1/2\gamma$	III	$0.20^{+0.70}_{-0.06}$	1	707	16.9	$*$
		$0/1$–2γ	IV	$0.14^{+0.70}_{-0.06}$	0	1456	34.2	$*$
$\nu_\tau 3h(n\pi^0)$	DIS	$3h$	I	2.61 ± 0.99	2	170	4.0	
		$3h$	II	0.58 ± 0.57	0	139	3.4	
		$3h$	III	0.86 ± 0.57	0	74	1.7	
		$3h$	IV	0.55 ± 0.59	1	309	7.6	
		$3h$	V	$0.32^{+0.57}_{-0.32}$	0	675	16.6	$*$

the $3h$ topology, the signal bins use also $\ln\lambda^{\mathrm{IN}}$ as a third dimension, since the higher multiplicity enhances the effect of the internal τ_{V} structure on background rejection. The last bin along $\ln\lambda^{\mathrm{NC}}$ is thus further divided into three bins along $\ln\lambda^{\mathrm{IN}}$ and $\ln\lambda^{\mathrm{CC}}$, respectively.

Table 1 summarizes the analysis flow on the various samples. The signal region is defined as $\ln\lambda^{\mathrm{CC}} > 3.5, 0, 0, 0$ and $\ln\lambda^{\mathrm{NC}} > 5.5, 6.0, 5.5, 4.0$ for the 0γ, 1γ, 2γ and $3h$ topologies, respectively. The absence of a τ_{V} internal structure necessitates a tighter constraint on $\ln\lambda^{\mathrm{CC}}$ for the 0γ topology. In the $3h$ decays, due to the large a_1 mass, a smaller phase space is available for the final state ν_τ, thus increasing the effectiveness of the $\ln\lambda^{\mathrm{NC}}$ cut. The final signal efficiency is similar for all topologies (Table 1). All signal bins are listed in Table 2.

6. Reliability of the background estimate

Since a τ signal would appear as a statistically significant excess of events inside the signal region, a crucial point for the analysis is the control of background predictions in this region. This requires two distinct steps. First, corrections to the Monte Carlo are extracted from the data themselves. Then, data control samples are used to check final predictions and to evaluate the corresponding systematic uncertainties.

6.1. Data simulator corrections

The procedure to evaluate the backgrounds is based upon the data simulator method (Section 4.2), which implies the application of the full selection scheme to appropriate data (DS) and simulated (MCS) samples. However, the overall background is actually composed of three different physical sources: NC, ν_μ ($\bar{\nu}_\mu$) CC and ν_e ($\bar{\nu}_e$) CC interactions (Table 1). In order to obtain a precise background evaluation, these three categories are considered separately:

- The NC correction is obtained from *identified* ν_μ CC interactions, by the removal of the leading muon. This results in hadronic systems of different charge distribution than genuine NC events. This charge bias is corrected for by selecting τ_V of both positive and negative charge and by averaging the two results.
- The ν_μ ($\bar{\nu}_\mu$) CC correction takes into account two distinct effects: the muon identification efficiency (veto) and the actual kinematic selection. The first correction factor is measured from a large sample ($\sim 6 \times 10^6$) of muons originating from a nearby beam and crossing the NOMAD detector. The kinematic correction factor is evaluated from *identified* ν_μ CC interactions in which the identification of the leading muon is ignored and, instead, the full τ selection is performed. The topological bias related to unidentified muons (muon chamber acceptance, low muon momenta) has little effect since this class of events is efficiently rejected by the kinematic veto (Section 5.3.1) and is checked through an appropriate CC control sample (Section 6.2).
- The ν_e ($\bar{\nu}_e$) CC correction is obtained from events *identified* as ν_e CC in the $\tau \to e\bar{\nu}_e\nu_\tau$ DIS search [7]. These events are then passed through the full event selection by ignoring the lepton identification. The electron identification (veto) used in the analysis, mainly based on TRD requirements, was independently checked using a sample of high-energy δ rays produced in the DC volume by muons originating from the nearby beam. As explained in Section 5.3.2, unidentified ν_e ($\bar{\nu}_e$) CC do not have specific topologies. Therefore, the described correction is adequate for all kinematic configurations.

The total net correction factors, $\epsilon_{DS}/\epsilon_{MCS}$, to the number of background events computed from the Monte Carlo are 1.8 for 0γ, 2.0 for 1γ, 1.3 for 2γ and 1.1 for $3h$ topologies, respectively. These numbers are integrated over the whole signal region and are dominated by the data simulator corrections of the NC samples. In the most sensitive kinematic region, characterized by only a small residual CC background (Table 5), the corresponding

correction factors are 0.70 for 0γ, 0.91 for 1γ, 0.96 for 2γ and 0.99 for $3h$ topologies, respectively.

The data simulator corrections computed for ν_τ CC events are 0.86 for single prong and 0.99 for three prong events and are essentially independent of the values of the likelihood ratios.

6.2. Control samples

The definition of appropriate control samples, which are needed to validate the final background predictions, must take into account two problems. First, the possibility to independently check each of the individual background contributions is desirable and requires, in turn, the ability to discriminate among them. In addition, the statistical uncertainty associated with each control sample must be small in order to provide a significant test of systematic effects.

The selection scheme based on two distinct likelihood functions provides by construction a separation between NC and CC backgrounds. Therefore, the required control samples can be defined in a natural way by selecting different regions in the plane of Fig. 7. Since $\ln\lambda^{\mathrm{CC}}$ is built only from the ν_μ CC sample, this latter background can be further partially decoupled from ν_e CC interactions in the plane of Fig. 7. This is important since in the low-background region essentially only ν_e ($\bar{\nu}_e$) CC events are present. However, for the sake of clarity, we will regroup backgrounds into NC and CC (ν_μ and ν_e) interactions in the following, unless otherwise specified.

The CC control sample is defined by analysing the projection along $\ln\lambda^{\mathrm{NC}}$ of events which fail at least one of the following selection criteria:

- lepton veto;
- $\ln\lambda^{\mathrm{IN}}$ cut;
- $\ln\lambda^{\mathrm{CC}}$ cut.

At large values of $\ln\lambda^{\mathrm{NC}}$ this sample is completely dominated by CC interactions, as can be seen from Fig. 9a, b.

Conversely, the NC control sample is defined by analysing the projection along $\ln\lambda^{\mathrm{CC}}$ of the events which fail the $\ln\lambda^{\mathrm{NC}}$ cut, after applying all the remaining cuts. Fig. 10 shows the statistical significance of the individual NC and CC contributions to this sample (see also Fig. 11).

In addition, the distributions of $\ln\lambda^{\mathrm{NC}}$ for the τ^+ sample, where no signal is expected because of the small $\bar{\nu}_\mu$ content of the beam (Section 3), are compared with data for each

Fig. 9. [On next page] Cumulative $\ln\lambda^{\mathrm{NC}}$ distributions in control samples for the 0γ, 1γ, 2γ and $3h$ topologies (from left to right): (a) after cuts on the structure of the hadronic system H (Section 5.2); (b) CC control samples complementary to the signal region; (c) final distribution outside the signal region (difference between the previous two); (d) wrong sign analysis. The histograms represent the individual NC and CC contributions to the total background. The vertical lines show the starting point of the signal region (solid) and of the last signal bin (dashed). The region to the right of the vertical solid lines in plots (a) and (b) is used to estimate the systematic uncertainties on the CC sample (region A of Fig. 7).

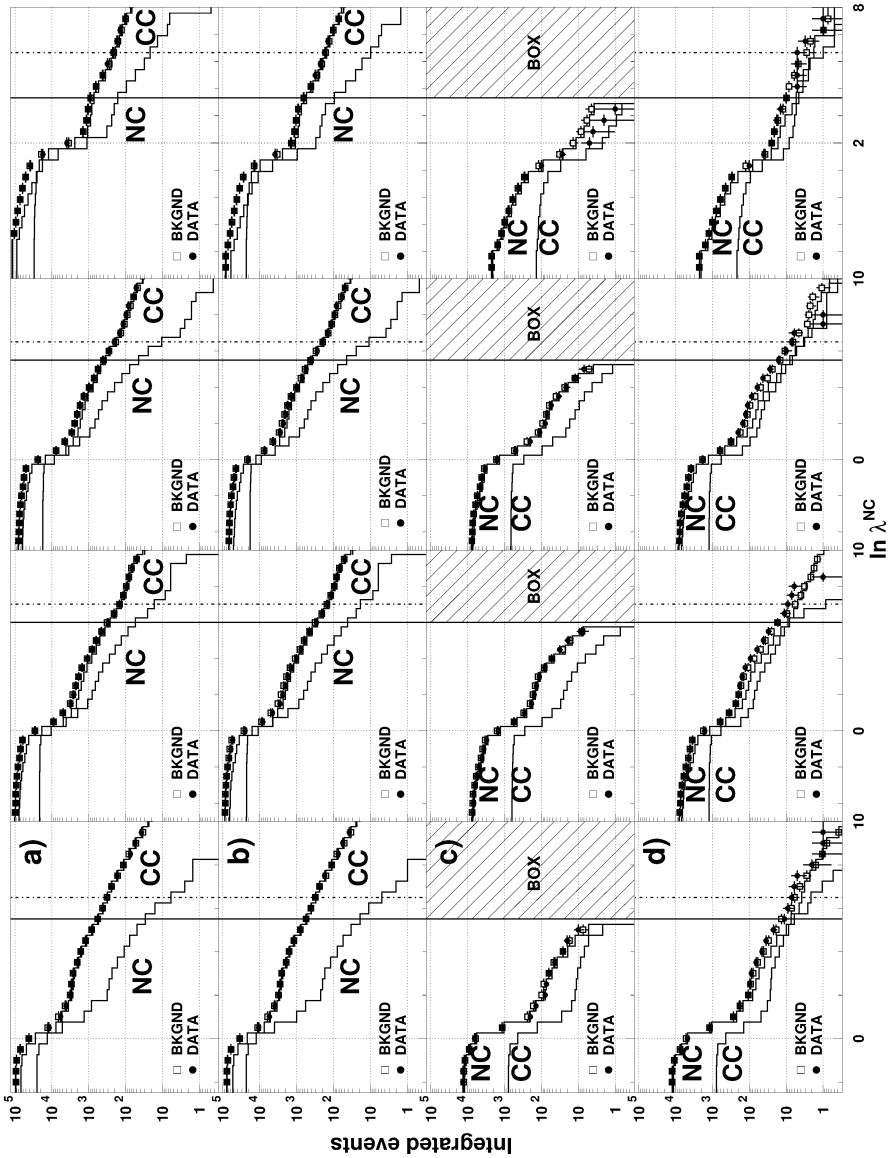
a)
b)
c)
d)
NC
CC
BOX
BKGND
DATA
Integrated events
ln λ^NC

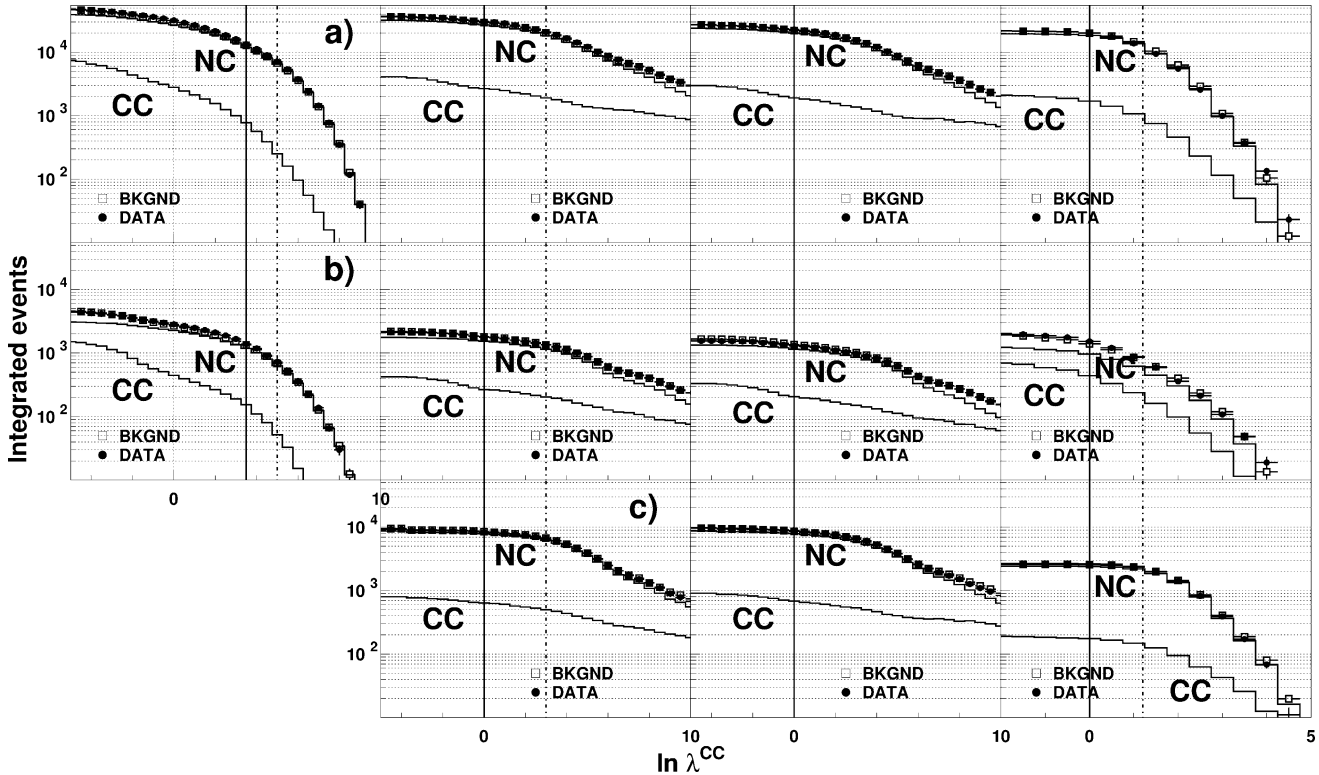

Fig. 10. Cumulative $\ln\lambda^{CC}$ distributions of data (full circles) and background predictions (open squares) in NC control samples for the 0γ, 1γ, 2γ and $3h$ (from left to right) topologies: (a) without cuts on $\ln\lambda^{NC}$ and $\ln\lambda^{IN}$; (b) with a $\ln\lambda^{NC}$ cut reducing the overall background by more than a factor of 10 but without $\ln\lambda^{IN}$ cut; (c) with $\ln\lambda^{IN} > 0.5, 0.0, 0.0$ (signal selection) but without $\ln\lambda^{NC}$ cut. The histograms represent the individual NC and CC contributions to the total background. The vertical lines show the starting point of the signal region (solid) and of the last signal bin (dashed). The region to the right of the vertical solid lines is used to estimate the systematic uncertainties on the NC sample (region B of Fig. 7).

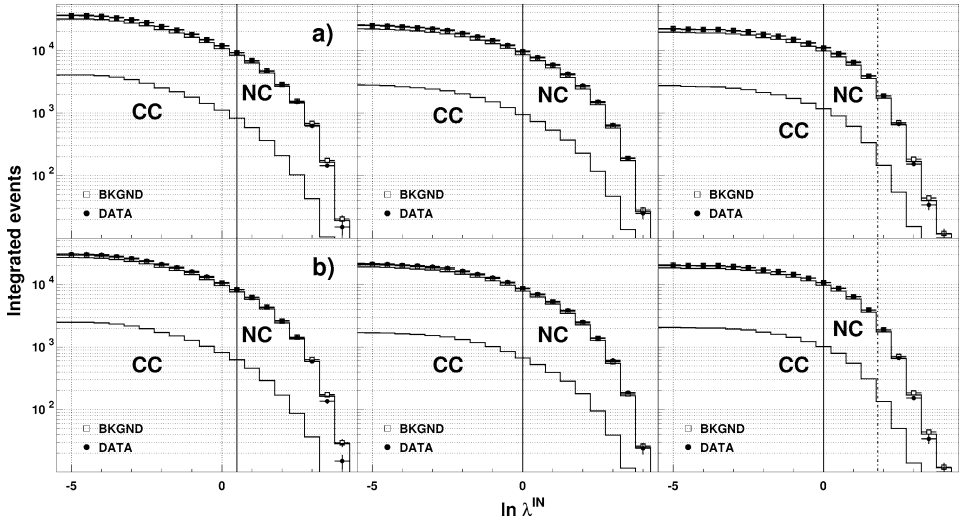

Fig. 11. Cumulative $\ln\lambda^{\mathrm{IN}}$ distributions of data (full circles) and background predictions (open squares) for the 1γ, 2γ and $3h$ (from left to right) topologies: (a) without cut on $\ln\lambda^{\mathrm{CC}}$; (b) with $\ln\lambda^{\mathrm{CC}} > 0.0, 0.0, 0.0$ (signal selection). The histograms represent the individual NC and CC contributions to the total background. The vertical lines show the starting point of the signal region (solid) and of the last signal bin for $3h$ events (dashed). The region to the right of the vertical solid lines is used to estimate the systematic uncertainties.

of the individual steps of Table 1. A similar check is performed in the τ^- search for the initial selection and for events outside the signal region (Fig. 9). Due to the charge bias of the lepton tagging procedure (Section 5.3) and, consequently, of kinematics (Section 5.5), the τ^+ selection is less effective than the τ^- search in rejecting backgrounds (Table 1). This gives the possibility to check background predictions with larger statistics.

Data events are in good agreement with background predictions for all control samples, as shown in Table 1, Figs. 9, 10 and 11. This gives confidence in the background estimation procedures and allows at the same time an evaluation of the systematic uncertainties.

7. Systematic uncertainties

The use of likelihood functions incorporating the full event topology provides a better estimate of systematic uncertainties with respect to a selection based on the application of a sequence of cuts. Moreover, the separation between CC and NC backgrounds gives additional high statistics control samples to constrain background predictions, as described in Section 6.2. This results, in turn, in a more precise background estimation.

7.1. Background

The systematic uncertainties on the number of background events predicted inside the signal region can be divided into two contributions, related to the overall normalization and

to the shape of the likelihood ratios.

The first term is estimated from a comparison of the total number of data and background events in both τ^+ and τ^- searches as a function of the selection criteria. This results in a r.m.s. of 1.9% from the differences in the last columns of Table 1. This value includes uncertainties related to fluxes, cross-sections and to the effect of the selection cuts for ν_μ CC interactions, which define the normalization, and NC events, which are the dominant background sample. For the remaining components (different from ν_μ) there is an additional systematic uncertainty coming from the integral flux predictions [12]. An upper limit on this contributions is obtained from the average systematic uncertainties on the corresponding energy spectra, which amount to 5.1%, 8.5% and 12.0% for ν_e, $\bar{\nu}_\mu$ and $\bar{\nu}_e$ CC interactions, respectively.

The second term is evaluated from the two control regions shown in Fig. 7 for CC (region A) and NC (region B) backgrounds, respectively. This is obtained by analyzing the corresponding control samples, defined in Section 6.2 as the event projections along each of the two likelihood ratio axes (Figs. 10 and 9a, b). The systematic uncertainty is then estimated as the r.m.s. of the distribution of differences between data and predictions *inside the signal region* of each control sample. This procedure is based on the assumption that in the region A (region B) a $\ln\lambda^{\mathrm{CC}}$ ($\ln\lambda^{\mathrm{NC}}$) cut does not introduce discrepancies between data and predictions which are dependent on the $\ln\lambda^{\mathrm{NC}}$ ($\ln\lambda^{\mathrm{CC}}$) distribution. Due to the limited rejection factor of the $\ln\lambda^{\mathrm{CC}}$ cut (Table 1), this condition is fulfilled by the CC control sample and the resulting number (5.5%) thus provides the final uncertainty on the CC background shape.

The tighter constraint imposed on $\ln\lambda^{\mathrm{NC}}$ requires additional checks of the effect of this variable on the $\ln\lambda^{\mathrm{CC}}$ distributions in region B. This is achieved by comparing the level of the observed agreement with different cuts on $\ln\lambda^{\mathrm{NC}}$, chosen in such a way as to reduce the overall background by more than a factor of 10 with respect to the initial value (Fig. 10a, b). Since the τ_{V} structure embedded in $\ln\lambda^{\mathrm{IN}}$ is almost independent of the global kinematics (apart from an overall boost factor in the laboratory frame), the cut on $\ln\lambda^{\mathrm{IN}}$ is not applied, in order to increase the available statistics and to have a consistent comparison of all topologies. The effect of the $\ln\lambda^{\mathrm{IN}}$ constraint is then checked separately, with no cut on $\ln\lambda^{\mathrm{NC}}$ (Fig. 10c). In addition, all the $\ln\lambda^{\mathrm{IN}}$ distributions for backgrounds are compared with data with and without the $\ln\lambda^{\mathrm{CC}}$ cut (Fig. 11). The final systematic uncertainty (r.m.s.) inside the signal region is estimated to be 4.1% from all these control samples.

Table 3 summarizes the individual contributions to systematic uncertainties, which, added in quadrature, result in a total systematic uncertainty of 5.8% for ν_μ CC, 10.3% for $\bar{\nu}_\mu$ CC, 7.6% for ν_e CC, 13.3% for $\bar{\nu}_e$ CC, and 4.5% for NC, respectively. However, the effect of this latter contribution is negligible since only the CC background is present in the most sensitive region of the analysis (Table 5). The overall net systematic uncertainty on the final background predictions for 0γ, 1γ, 2γ and $3h$ topologies is then 5.0%, 5.1%, 5.4% and 5.5% at the starting point of the signal region and 10.0%, 9.2%, 9.2% and 5.8% in the low background region. Given the large rejection factors of $\mathcal{O}(10^5)$ such a control of systematic uncertainties is noteworthy.

Table 3
Contributions to systematic uncertainties for background and signal events

Background	
Normalization	1.9%
Integral ν_e/ν_μ	5.1%
Integral $\bar{\nu}_\mu/\nu_\mu$	8.5%
Integral $\bar{\nu}_e/\nu_\mu$	12.0%
CC $\ln\lambda$ shape in signal region	5.5%
NC $\ln\lambda$ shape in signal region	4.1%
Signal	
Normalization	1.9%
σ_τ/σ_μ	3.0%
$\ln\lambda$ shape in signal region	5.0%

7.2. Signal

The probability of oscillation, $P_{\rm osc}$, is estimated as the ratio between the number of observed τ events and the maximal number of signal events expected if all incident ν_μ had converted into ν_τ (Section 8.3). For the $\nu_\mu \to \nu_\tau$ oscillation, neglecting a term $\mathcal{O}(P_{\rm osc}^2)$, this last quantity is defined by:

$$N_\tau^{\mu\tau} = N_\mu^{\rm obs} \times (\epsilon_\tau/\epsilon_\mu) \times (\sigma_\tau/\sigma_\mu) \times {\rm Br}, \tag{1}$$

where:

- $N_\mu^{\rm obs}$ is the observed number of ν_μ CC interactions (Section 1). The number of ν_μ CC interactions corresponding to the LM topologies are evaluated to be 11% of the total [7].
- ϵ_τ and ϵ_μ are the detection efficiencies for τ signal events and ν_μ CC events, respectively, integrated over the incident ν_μ spectrum. The cuts used to select $N_\mu^{\rm obs}$ and ϵ_μ vary from channel to channel in order to reduce systematic uncertainties in the ratio $\epsilon_\tau/\epsilon_\mu$ for that channel.
- σ_τ/σ_μ is the suppression factor of the ν_τ cross section due to the difference between the τ and μ masses, averaged over the incident ν_μ spectrum. For the ν_μ spectrum used in this experiment [12] and for an energy-independent oscillation probability (corresponding to the large Δm^2 hypothesis), it is evaluated to be 0.48, 0.60 and 0.82 for the deep inelastic, resonance and quasielastic processes. The resulting average values for the DIS and LM analyses are 0.48 and 0.57, respectively. The event sample selected by the LM analyses contains significant fractions of DIS events satisfying the LM selection [7].
- Br is the branching ratio for the τ decay channel under consideration.

The systematic uncertainty on the overall normalization for the signal sample is common to the ν_μ CC background (1.9%) and includes the effect of the individual

selection criteria listed in Table 1. The maximum Data Simulator correction applied to the signal likelihood shapes, decoupled from the overall normalization, is 5.0%. We use this maximum correction as the systematic uncertainty on the signal shape.

The uncertainty on the suppression factor σ_τ/σ_μ, which will also contribute to the overall systematic uncertainty, is due to the uncertainties on the ν_μ energy spectrum and on the structure functions used in the computation. It is estimated to be 3.0%. The uncertainty on the τ branching ratios is negligible [25].

The final systematic uncertainty on the signal sample is 6.1% from the sum in quadrature of all the individual contributions summarized in Table 3.

8. Results

8.1. Analysis of the signal region

After the choice of the selection criteria and the cross-check of the background predictions, we analyze data events falling in the signal region of the hadronic DIS channels (the blind box). Data events populate the various bins in a manner consistent with backgrounds, as summarized in Table 2. The overall integrals and shapes of the final $\ln\lambda$ distributions are in good agreement with background predictions (Fig. 12). Therefore, no signal from oscillations is observed.

8.2. Combined results

The overall NOMAD results are obtained from the combination of the new analysis of the hadronic τ decays with the $\nu_\tau e\bar{\nu}_e$ DIS and the LM analyses described in Ref. [7] (Appendix B). Table 4 lists all the individual contributions and the corresponding sensitivities. The unified analysis of $\nu_\tau h(n\pi^0)$ topologies described in the present paper is the most sensitive ν_τ appearance search in NOMAD.

As discussed in Section 5.5, the strength of this search lies in the possibility to define, through kinematic constraints, large regions characterized by the expectation of low background. A precise control of background predictions using the data themselves is also crucial. The major low background (< 0.5 events) bins are summarized in Table 5. Overall, these bins contribute about 75% of the total sensitivity of the experiment. A single event is observed within this kinematic region. This event, shown in Fig. 13, is classified as a $\tau \to \nu_\tau\rho$ candidate and has large values of all likelihood ratios (Fig. 12b, c).

The overall systematic uncertainties for the hadronic DIS channels are given in Section 7. For the remaining modes the estimated systematic uncertainties are 20% and 10% on backgrounds and $N_\tau^{\mu\tau}$, respectively [7].

8.3. Evaluation of confidence regions

The final result of the measurement is expressed as a frequentest confidence interval [27] which accounts for the fact that each τ decay mode and signal bin (Tables 2 and 6) may

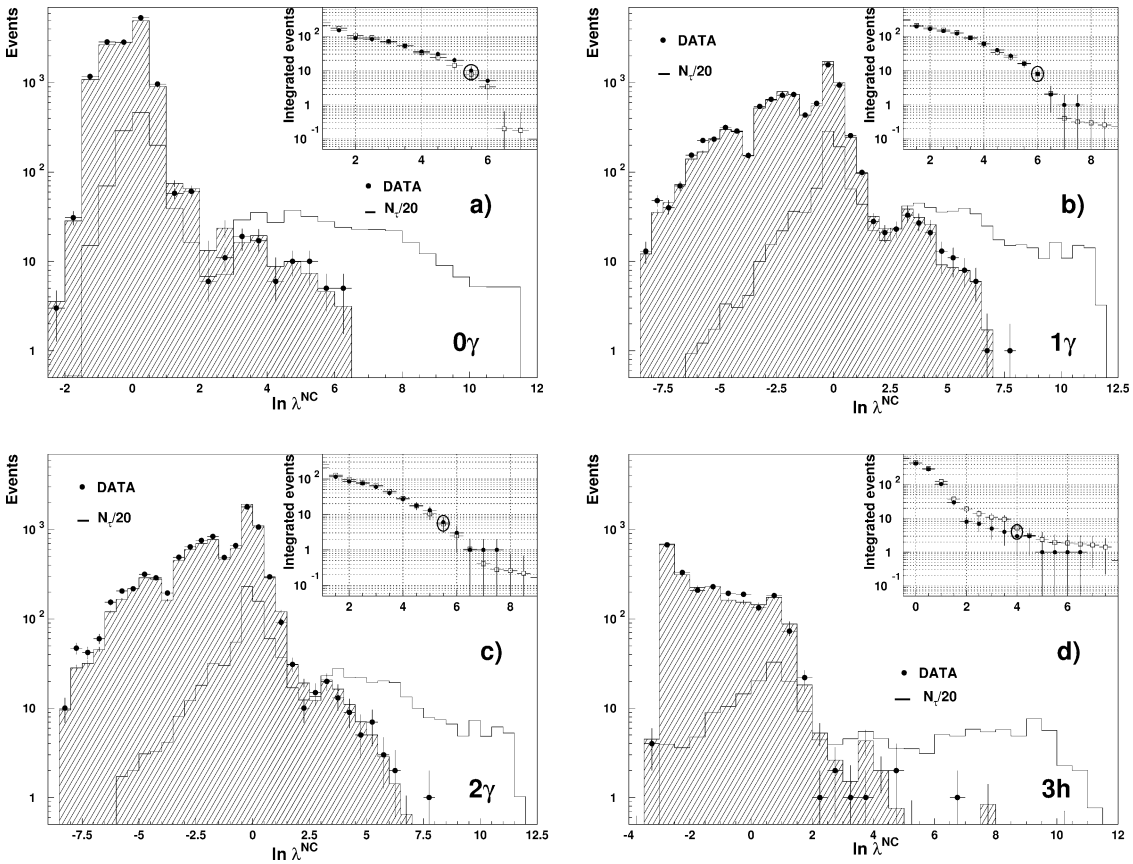

Fig. 12. Histograms of $\ln \lambda^{NC}$ for events passing all cuts except the cut on $\ln \lambda^{NC}$ in (a) 0γ, (b) 1γ, (c) 2γ and (d) $3h$, for data (points with statistical error bars), total backgrounds (shaded) and $N_\tau^{\mu\tau}$ (Section 7.2), scaled down by a factor 20 (unshaded). The insets give, for each value of $\ln \lambda^{NC}$, the total number of events beyond that value, for data (dots) and expected background (squares); the encircled points are at the boundary of the signal regions.

Table 4
Summary of backgrounds and efficiencies for all the individual τ searches. The columns labelled τ^- summarize the observed number of τ^- candidate events (Obs) and the corresponding predicted background (Tot Bkgnd) for the sum of all bins in the signal region. The columns labelled τ^+ contain the equivalent numbers for the positive control sample. The corresponding τ^- selection efficiencies (ϵ_τ), not including branching ratios, and the $N_\tau^{\mu\tau}$ and $N_\tau^{e\tau}$ (Sections 7.2 and 8.3) are also listed. For the LM topologies the quoted ϵ_τ is the average efficiency for quasi-elastic and resonance events. The last column shows the overall sensitivity of each individual τ search, based on the combination of all signal bins

Analysis		τ^-		τ^+		ϵ_τ(%)	$N_\tau^{\mu\tau}$	$N_\tau^{e\tau}$	$S_{\mu\tau}$
		Obs	Tot Bkgnd	Obs	Tot Bkgnd				($\times 10^{-4}$)
$\nu_\tau \bar{\nu}_e e$	DIS	5	$5.3^{+0.7}_{-0.5}$	9	8.0 ± 2.4	3.6	4318	88.0	8.0
$\nu_\tau h(n\pi^0)$	DIS	21	19.5 ± 3.5	44	44.9 ± 4.6	2.2	7522	177.4	4.0
$\nu_\tau 3h(n\pi^0)$	DIS	3	4.9 ± 1.5	10	9.9 ± 1.6	1.3	1367	33.3	22.2
$\nu_\tau \bar{\nu}_e e$	LM	6	5.4 ± 0.9	3	2.2 ± 0.5	6.3	864	8.8	55.2
$\nu_\tau h(n\pi^0)$	LM	12	11.9 ± 2.9	40	44.1 ± 9.2	1.9	857	16.7	88.9
$\nu_\tau 3h(n\pi^0)$	LM	5	3.5 ± 1.2	1	2.2 ± 1.1	2.0	298	5.2	161.0

Table 5
Summary of background and data events in the low background bins. The corresponding $N_\tau^{\mu\tau}$ and $N_\tau^{e\tau}$, as defined in Sections 7.2 and 8.3, are listed in the last two columns. The quoted background consists mainly of ν_e CC events for the $\nu_\tau e \bar{\nu}_e$ channel; of a mixture of ν_e and $\bar{\nu}_e$ CC events for the $\nu_\tau h(n\pi^0)$ channel and of ν_μ CC events for the $\nu_\tau 3h(n\pi^0)$ channel. The errors include contributions from the remaining sources

Analysis			Bin #	Tot Bkgnd	Data	$N_\tau^{\mu\tau}$	$N_\tau^{e\tau}$
$\nu_\tau e \bar{\nu}_e$	DIS		III	$0.18^{+0.18}_{-0.08}$	0	680	15.0
			VI	0.16 ± 0.08	0	1481	32.7
	($E_{\rm vis} < 12$ GeV)		II+III+VI	0.27 ± 0.13	0	665	8.7
$\nu_\tau h(n\pi^0)$	DIS	0γ	III	$0.05^{+0.60}_{-0.03}$	0	288	6.9
		0γ	IV	$0.12^{+0.60}_{-0.05}$	0	1345	31.1
		1γ	III	$0.07^{+0.70}_{-0.04}$	0	223	5.7
		1γ	IV	$0.07^{+0.70}_{-0.04}$	0	1113	26.6
		2γ	IV	$0.11^{+0.60}_{-0.06}$	0	211	4.9
		$1/2\gamma$	III	$0.20^{+0.70}_{-0.06}$	1	707	16.9
		$0/1$–2γ	IV	$0.14^{+0.70}_{-0.06}$	0	1456	34.2
$\nu_\tau 3h(n\pi^0)$	DIS	$3h$	V	$0.32^{+0.57}_{-0.32}$	0	675	16.6
Total				$1.69^{+1.85}_{-0.39}$	1	8844	199.3

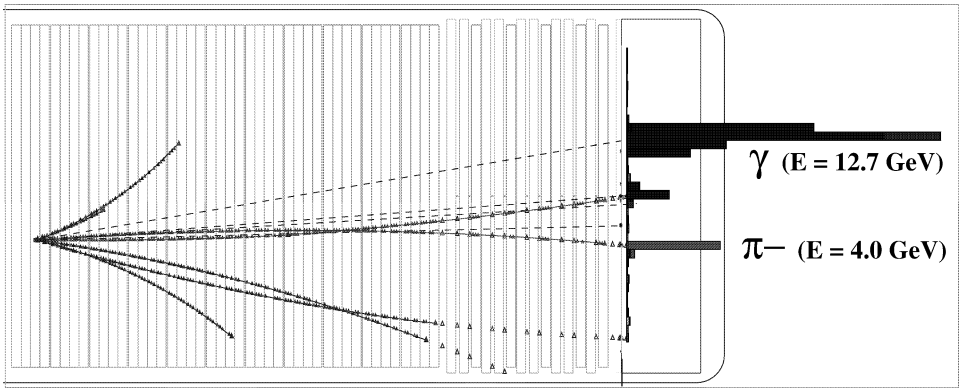

Fig. 13. Data event (run 14162, event 25050) falling in the low background signal region of Table 5. The event is classified as $\tau \to \rho\nu_\tau$ (bin $1/2\gamma$ III) decay candidate: $\ln\lambda^{\mathrm{IN}} = 2.1$, $\ln\lambda^{\mathrm{CC}} = 9.4$ and $\ln\lambda^{\mathrm{NC}} = 7.5$. Solid lines represent the reconstructed charged tracks (open triangles show their extrapolation) whereas dashed lines represent the ECAL neutral clusters. The energy deposition of individual ECAL cells is also shown by the shaded bins on the right.

have a different signal to background ratio. The acceptance region of Ref. [27] therefore becomes multidimensional to contain each of the separate measurements. The procedure follows the prescription of Ref. [25]. This computation [26] takes into account the number of observed signal events, the expected background and its uncertainty, and the maximal number of the expected signal events.

The resulting 90% CL upper limit on the $\nu_\mu \to \nu_\tau$ oscillation probability is:

$$P_{\mathrm{osc}}(\nu_\mu \to \nu_\tau) < 1.63 \times 10^{-4}. \tag{2}$$

Under a two-neutrino family formalism this corresponds to $\sin^2 2\theta_{\mu\tau} < 3.3 \times 10^{-4}$ for large Δm^2 and to the exclusion region in the Δm^2–$\sin^2 2\theta$ plane shown in Fig. 14. The result is significantly more stringent than the previously published limits [7,20–23]. The sensitivity [27] of the experiment is $P_{\mathrm{osc}} = 2.5 \times 10^{-4}$; this is higher than the quoted confidence limit, since the number of observed events is smaller than the estimated background. In the absence of signal events, the probability to obtain an upper limit of 1.63×10^{-4} or lower is 37% (Fig. 15). This result matches the design sensitivity of the experiment ($P_{\mathrm{osc}} = 1.9 \times 10^{-4}$).

In the context of a two-flavour approximation, we can reinterpret the result in terms of $\nu_e \to \nu_\tau$ oscillations, by assuming that any observed ν_τ signal should be due to oscillations from the small ν_e component of the beam [28]. The corresponding maximal number of signal events, $N_\tau^{e\tau}$, is then obtained from $N_\tau^{\mu\tau}$ by reweighting the signal events using the ν_e to ν_μ flux ratio. This procedure introduces a further systematic uncertainty of 4.7% on the values of $N_\tau^{e\tau}$, related to flux predictions [12]. The resulting 90% CL upper limit on the $\nu_e \to \nu_\tau$ oscillation probability is then:

$$P_{\mathrm{osc}}(\nu_e \to \nu_\tau) < 0.74 \times 10^{-2} \tag{3}$$

corresponding to $\sin^2 2\theta_{e\tau} < 1.5 \times 10^{-2}$ for large Δm^2. The exclusion region in the Δm^2–$\sin^2 2\theta$ plane is also shown in Fig. 14. The $\nu_e \to \nu_\tau$ sensitivity is $P_{\mathrm{osc}} = 1.1 \times 10^{-2}$ and

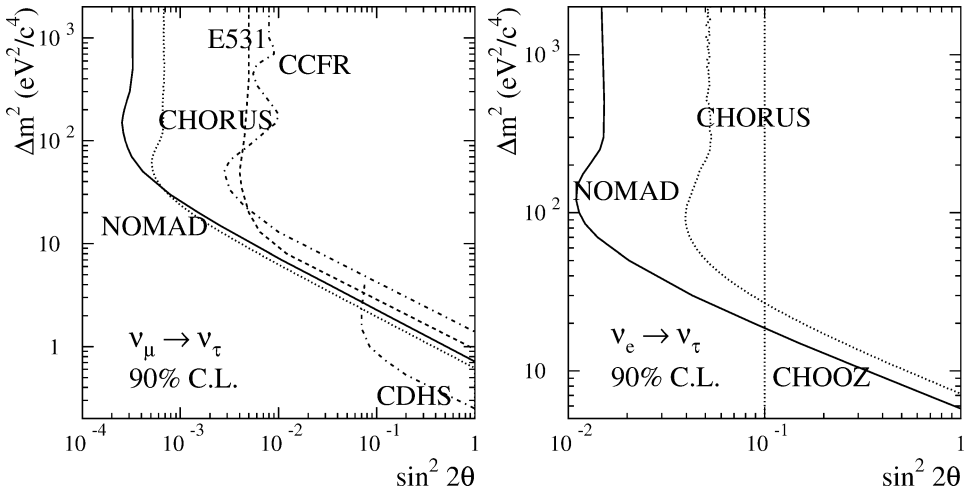

Fig. 14. Contours outlining a 90% CL region in the Δm^2–sin$^2\,2\theta$ plane for the two-family oscillation scenario. The NOMAD $\nu_\mu \to \nu_\tau$ (left) and $\nu_e \to \nu_\tau$ (right) curves are shown as solid lines, together with the limits published by other experiments [20–24].

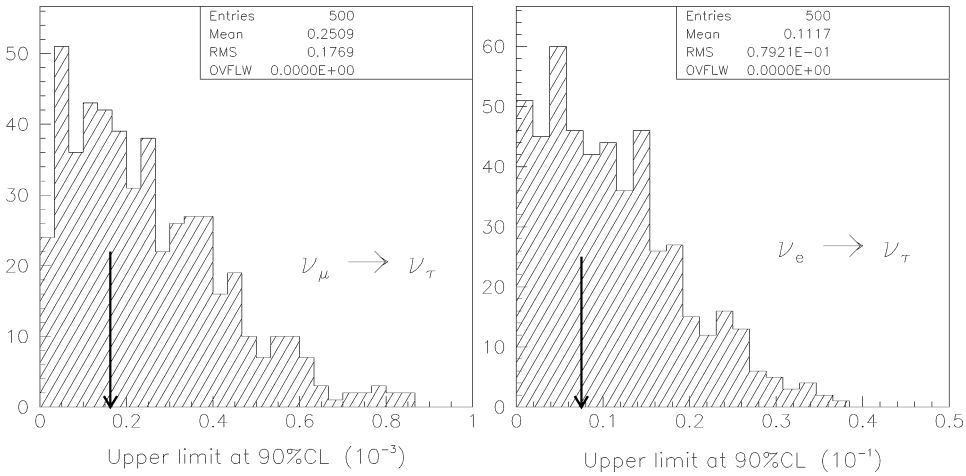

Fig. 15. Histograms of the upper limits obtained, in the absence of signal events, for 500 simulated experiments with the same NOMAD expected background [27]. The averages correspond to the quoted sensitivities while the arrows are the actual upper limits obtained from the data in the $\nu_\mu \to \nu_\tau$ (left) and $\nu_e \to \nu_\tau$ (right) searches.

the probability to obtain an upper limit of 0.74×10^{-2} or lower is 39% (Fig. 15). Both the sensitivity and the probability to obtain the result (goodness-of-fit) are an essential part of the limits themselves, as pointed out in Refs. [25,27].

The results from the τ appearance search also exclude effective couplings of ν_μ or ν_e with the τ lepton, which are equivalent to the oscillation probabilities at large Δm^2. In particular, this information is required in order to relate the recent observation of τ

production by the DONUT Collaboration [29] to the presence of ν_τ in the beam. At 99% CL the NOMAD data limit such couplings to $P_{\mu\tau} < 4.4 \times 10^{-4}$ and $P_{e\tau} < 2.0 \times 10^{-2}$.

9. Conclusions

The analysis of the full NOMAD data sample gives no evidence for ν_τ appearance. In the two-family oscillation formalism this result excludes a region of the $\nu_\mu \to \nu_\tau$ oscillation parameters which limits $\sin^2 2\theta_{\mu\tau}$ at high Δm^2 to values smaller than 3.3×10^{-4} at 90% CL, and Δm^2 to values smaller than $\Delta m^2 < 0.7$ eV$^2/c^4$ at $\sin^2 2\theta_{\mu\tau} = 1$. The corresponding excluded region at 90% CL for the $\nu_e \to \nu_\tau$ oscillation parameters includes $\sin^2 2\theta_{e\tau} < 1.5 \times 10^{-2}$ at large Δm^2 and $\Delta m^2 < 5.9$ eV$^2/c^4$ at $\sin^2 2\theta_{e\tau} = 1$. Our sensitivity to oscillations is not limited by backgrounds, but is essentially defined by the available statistics.

The NOMAD experiment has explored neutrino oscillations down to probabilities which are more than one order of magnitude smaller than limits set by the previous generation of experiments. For the first time, a purely kinematic approach has been applied to the detection of ν_τ CC interactions. Our final results demonstrate that this approach has developed into a mature technique, providing a precise control of backgrounds from the data themselves.

Acknowledgements

We thank the management and staff of CERN and of all participating institutes for their vigorous support of the experiment. Particular thanks are due to the CERN accelerator and beam-line staff for the magnificent performance of the neutrino beam. The following funding agencies have contributed to this experiment: Australian Research Council (ARC) and Department of Industry, Science, and Resources (DISR), Australia; Institut National de Physique Nucléaire et Physique des Particules (IN2P3), Commissariat à l'Energie Atomique (CEA), Ministère de l'Education Nationale, de l'Enseignement Supérieur et de la Recherche, France; Bundesministerium für Bildung und Forschung (BMBF, contract 05 6DO52), Germany; Istituto Nazionale di Fisica Nucleare (INFN), Italy; Russian Foundation for Basic Research, Institute for Nuclear Research of the Russian Academy of Sciences, Russia; Fonds National Suisse de la Recherche Scientifique, Switzerland; Department of Energy, National Science Foundation (grant PHY-9526278), the Sloan and the Cottrell Foundations, USA.

We also thank our secretarial staff, Jane Barney, Katherine Cross, Joanne Hebb, Marie-Anne Huber, Jennifer Morton, Rachel Phillips and Mabel Richtering, and the following people who have worked with the collaboration on the preparation and the data collection stages of NOMAD: M. Anfreville, M. Authier, G. Barichello, A. Beer, V. Bonaiti, A. Castera, O. Cloué, C. Détraz, L. Dumps, C. Engster, G. Gallay, W. Huta, E. Lessmann, J. Mulon, J.P. Passérieux, P. Petitpas, J. Poinsignon, C. Sobczynski, S. Soulié, L. Visentin, P. Wicht.

Appendix A. Kinematic variables

The event kinematics is based on a set of global variables which describe the general properties of the two momentum vectors of a *leading particle* and of the hadronic system H recoiling against it, in the laboratory frame. This convention is closely related to the kinematics of CC interactions. However, in general, any track (or system of tracks) can be chosen as leading particle.

Invariance with respect to an arbitrary rotation in the plane transverse to the beam direction means that an event can in fact be fully described by five degrees of freedom (Fig. 16): three in the transverse plane (x, y) and two along the beam direction (z).

In the selection of ν_τ CC interactions, the leading particle consists of the visible τ decay product(s) $\tau_{\rm V}$. The following kinematic variables can then be computed (Fig. 16):

- $\mathbf{p}_{\rm vis}$, the total visible momentum of the event. This is computed by summing the momenta of all primary charged particles, neutral secondary vertices and neutral ECAL clusters.
- $E_{\rm vis}$, the total visible energy of the event.
- $\mathbf{p}^{\tau_{\rm V}}$ and $\mathbf{p}^H$, the total momentum of the *visible* tau decay product(s) and of the associated hadronic system, respectively, such that $\mathbf{p}^{\tau_{\rm V}} + \mathbf{p}^H = \mathbf{p}_{\rm vis}$.
- y_{Bj}, the ratio between p^H and the total visible energy.
- $\mathbf{p}_T^{\tau_{\rm V}}$ and $\mathbf{p}_T^H$, the components of $\mathbf{p}^{\tau_{\rm V}}$ and $\mathbf{p}^H$ perpendicular to the neutrino beam direction.
- $\mathbf{p}_T^m$, defined as $-(\mathbf{p}_T^{\tau_{\rm V}} + \mathbf{p}_T^H)$ and interpreted as a measurement of the "missing" transverse momentum due to the neutrino(s) from τ decay.
- M_T, the transverse mass, given by $M_T^2 = 4 p_T^{\tau_{\rm V}} p_T^m \sin^2(\phi_{\tau_{\rm V} m}/2)$ where $\phi_{\tau_{\rm V} m}$ is the angle between $\mathbf{p}_T^{\tau_{\rm V}}$ and $\mathbf{p}_T^m$, when assuming massless decay product(s). For τ events, $M_T \leqslant \tau$ mass, up to detector resolution and Fermi motion effects.

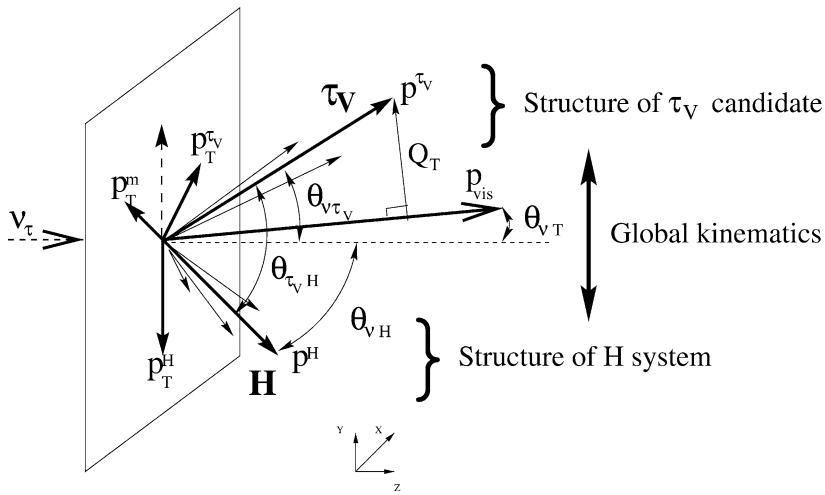

Fig. 16. Definition of the NOMAD kinematics for a ν_τ CC event.

- R_{pT}, the ratio of the transverse momentum $p_T^{\tau_V}$ and the missing transverse momentum p_T^m.
- Q_T, the component of $\mathbf{p}^{\tau_V}$ perpendicular to the total visible momentum vector (including τ_V).
- Q_{Lep}, the component of a charged particle momentum perpendicular to the total momentum of the rest of the event.
- $\theta_{\nu H}$, the angle between the neutrino beam direction and the hadronic system.
- $\theta_{\nu\tau_V}$, the angle between the neutrino beam direction and the τ_V momentum vector.
- $\theta_{\nu T}$, the angle between the neutrino beam direction and the total visible momentum vector of the event.
- $\theta_{\tau_V H}$, the angle between the hadronic system and τ_V.

For the lepton tagging algorithms (Section 5.3) and the kinematic rejection of CC interactions (Section 5.5) the lepton candidate track l_{CC}^{μ} is chosen as leading particle in the computation of all the above variables (e.g., $\theta_{\nu\tau_V}$ becomes $\theta_{\nu l}$ etc.).

The following variables, partially related to the previous ones, incorporate information from the internal structure of the hadronic system H:

- $\theta_{\tau_V h_i}$, the minimum angle between τ_V and any other primary track h_i in the event.
- $\langle Q_T^2\rangle_H$, average Q_T^2 computed among all the charged tracks of the remaining hadronic system H, after the exclusion of a particular track. This variable measures the transverse size of the hadronic system.
- $\langle Q_T^2\rangle_T$, average Q_T^2 computed among all the charged tracks in the event.
- R_{Q_T}, ratio between the transverse size of the hadronic system, $\langle Q_T^2\rangle_H$, and that of the full event, $\langle Q_T^2\rangle_T$. This variable is sensitive to the isolation of the particle(s) not included in the hadronic system H.
- $\Delta r_{\tau_V h_i} = \sqrt{(\Delta\eta_{\tau_V h_i})^2 + (\Delta\phi_{\tau_V h_i})^2}$, the minimum invariant opening cone between τ_V and any other primary track h_i in the event. This combines the differences of the corresponding angles in the transverse plane ϕ and of the pseudo-rapidity $\eta = -\ln\tan(\theta/2)$.

In addition, variables describing the internal structure of the candidate τ_V are used, where applicable, in order to increase background rejection:

- M_ρ, invariant mass of a $\pi^-\pi^0$ combination.
- M_{ρ^0}, invariant mass of a $\pi^-\pi^+$ combination.
- M_{π^0}, invariant mass of a $\gamma\gamma$ combination.
- M_{a_1}, invariant mass of a $\pi^-\pi^+\pi^-$ combination.
- $\theta_{\pi^-\pi^0}$, opening angle between a π^- and a π^0. The π^0 momentum can be obtained, in turn, from a single ECAL cluster (1γ) or from the sum of two separate ECAL clusters (2γ).
- $\theta_{\gamma\gamma}$, opening angle between two γ's.
- $\theta_{\pi^+\pi^-}$, opening angle between a π^+ and a π^-.
- $\theta_{\pi^-\pi^-}$, opening angle between two distinct π^-'s.
- E_{π^0}, energy of a π^0 obtained from a single ECAL cluster (1γ) or from the sum of two separate ECAL clusters (2γ).

- $E_{\gamma}^{\max}$, maximum energy between two different γ's used to reconstruct a π^0.
- E_{π^+}, energy of a π^+.
- E_{ρ^0}, energy of a $\pi^+\pi^-$ combination,

where the track charges refer to the τ^- selection (opposite for the τ^+ selection).

Appendix B. Additional topologies

In addition to the analysis of the hadronic DIS channels described in this paper, the ν_τ appearance search in NOMAD includes the analysis of the $\tau^- \to e^- \bar{\nu}_e \nu_\tau$ DIS decays and of the LM topologies from Ref. [7]. The corresponding values of $N_\tau^{\mu\tau}$ and $N_\tau^{e\tau}$ have been updated according to the most recent beam predictions [12]. Table 6 summarizes all the relevant numbers for these samples, which supersede the ones quoted in Ref. [7].

In principle, NOMAD is sensitive to all leptonic and hadronic τ decay channels. However, the $\tau^- \to \mu^- \bar{\nu}_\mu \nu_\tau$ decay channel is dominated by the ν_μ CC background where the primary muon is positively *identified* in the detector. In view of the intrinsic difficulty of the evaluation of the systematic uncertainty on this background, due to the absence of a suitable control sample, this channel is not directly used for the ν_τ search.

Table 6
Number of background and data events in the signal region for the $\tau^- \to e^- \bar{\nu}_e \nu_\tau$ DIS and LM topologies [7]. The corresponding $N_\tau^{\mu\tau}$ and $N_\tau^{e\tau}$, as defined in Sections 7.2 and 8.3, are listed in the last two columns. The bins denoted by a star are considered as low background bins (Section 8.2)

Analysis		Bin #	Tot Bkgnd	Data	$N_\tau^{\mu\tau}$	$N_\tau^{e\tau}$	
$\tau^- \to e^- \bar{\nu}_e \nu_\tau$	DIS	I	$0.85^{+0.26}_{-0.16}$	2	143	2.8	
($E_{\rm vis} > 12$ GeV)		II	$0.46^{+0.23}_{-0.12}$	1	136	2.9	
		III	$0.18^{+0.18}_{-0.08}$	0	680	15.0	*
		IV	1.85 ± 0.22	2	554	14.0	
		V	0.78 ± 0.15	0	406	9.1	
		VI	0.16 ± 0.08	0	1481	32.7	*
($E_{\rm vis} < 12$ GeV)		I+IV+V	0.77 ± 0.26	0	253	2.8	
		II+III+VI	0.27 ± 0.13	0	665	8.7	*
$\tau^- \to e^- \bar{\nu}_e \nu_\tau$	LM	I	3.09 ± 0.67	3	282	2.9	
		II	1.50 ± 0.41	2	286	2.9	
		III	0.82 ± 0.41	1	296	3.0	
$\tau \to h(n\pi^0)$	LM	ρ	5.2 ± 1.8	7	480	8.9	
	LM	h	6.7 ± 2.3	5	377	7.8	
$\tau \to 3h(n\pi^0)$	LM	–	3.5 ± 1.2	5	298	5.2	

References

[1] For a review of early solar neutrino data and their interpretation see S.A. Bludman et al., Nucl. Phys. B 31 (1993) 156.
[2] L. Wolfenstein, Phys. Rev. D 17 (1978) 2369;
S.P. Mikheyev, A.Yu. Smirnov, Nuovo Cimento C 9 (1986) 17.
[3] T. Yanagida, Prog. Theor. Phys. B 135 (1978) 66;
M. Gell-Mann, P. Ramond, R. Slansky, in: P. von Niewenhuizen, D. Freedman (Eds.), Supergravity, North Holland, Amsterdam, 1979, p. 315.
[4] NOMAD Collaboration, J. Altegoer et al., Nucl. Instrum. Methods A 404 (1998) 96.
[5] E. Eskut et al., Nucl. Instrum. Methods A 401 (1997) 7.
[6] C. Albright, R. Shrock, Phys. Lett. B 84 (1979) 123.
[7] NOMAD Collaboration, P. Astier et al., Phys. Lett. B 483 (2000) 387.
[8] M. Anfreville et al., hep-ex/0104012, submitted to Nucl. Instrum. Methods A.
[9] G. Bassompierre et al., Nucl. Instrum. Methods A 403 (1998) 363;
G. Bassompierre et al., Nucl. Instrum. Methods A 411 (1998) 63.
[10] D. Autiero et al., Nucl. Instrum. Methods A 372 (1996) 556;
D. Autiero et al., Nucl. Instrum. Methods A 373 (1996) 358;
D. Autiero et al., Nucl. Instrum. Methods A 387 (1997) 352;
D. Autiero et al., Nucl. Instrum. Methods A 411 (1998) 285;
D. Autiero et al., Nucl. Instrum. Methods A 425 (1999) 188.
[11] J. Altegoer et al., Nucl. Instrum. Methods A 428 (1999) 299.
[12] NOMAD Collaboration, P. Astier et al., Prediction of neutrino fluxes in the NOMAD experiment, paper in preparation.
[13] M.C. Gonzales-Garcia, J.J. Gomez-Cadenas, Phys. Rev. D 55 (1997) 1297;
B. Van de Vyver, Nucl. Instrum. Methods A 385 (1997) 91.
[14] G. Ingelman, LEPTO 6.1, in: W. Buchmueller, G. Ingelman (Eds.), Proc. of Physics at HERA, DESY, Hamburg, 1992, p. 1366.
[15] T. Sjöstrand, Comput. Phys. Commun. 39 (1986) 347;
T. Sjöstrand, M. Bengtsson, Comput. Phys. Commun. 43 (1987) 367;
T. Sjöstrand, Comput. Phys. Commun. 82 (1994) 74.
[16] A. Bodek, J. Ritchie, Phys. Rev. D 23 (1981) 1070.
[17] M. Glück, E. Reya, A. Vogt, Z. Phys. C 53 (1992) 127.
[18] H. Plothow-Besch, Comput. Phys. Commun. 75 (1993) 396.
[19] GEANT 3.21, CERN Program Library Long Writeup W5013.
[20] E531 Collaboration, N. Ushida et al., Phys. Rev. Lett. 57 (1986) 2897.
[21] CDHS Collaboration, F. Dydak et al., Phys. Lett. B 134 (1984) 281.
[22] CCFR Collaboration, K.S. McFarland et al., Phys. Rev. Lett. 75 (1995) 3993.
[23] CHORUS Collaboration, E. Eskut et al., Phys. Lett. B 497 (2001) 8.
[24] CHOOZ Collaboration, M. Apollonio et al., Phys. Lett. B 466 (1999) 415.
[25] Particle Data Group, Review of Particle Physics, Eur. Phys. J. C 15 (2000) 321.
[26] NOMAD Collaboration, P. Astier et al., Phys. Lett. B 453 (1999) 169.
[27] G.J. Feldman, R.D. Cousins, Phys. Rev. D 57 (1998) 3873.
[28] NOMAD Collaboration, P. Astier et al., Phys. Lett. B 471 (2000) 406.
[29] DONUT Collaboration, K. Kodama et al., Phys. Lett. B 504 (2001) 218.